

On the physical nature of the Wilson-Bappu effect: revising the gravity and temperature dependence

F. Rosas-Portilla^{1*}, K. -P. Schröder^{1,2}, D. Jack¹

¹*Departamento de Astronomía, Universidad de Guanajuato, Callejón de Jalisco S/N Col. Valenciana, Guanajuato 36023, México*

²*Sterrewacht Leiden, Universiteit Leiden, Nils Bohrweg 2, Leiden 2333CA, Netherlands*

Accepted XXX. Received YYY; in original form ZZZ

ABSTRACT

We present a sample of 32 stars of spectral types G and K, and luminosity classes I to V, with moderate activity levels, covering four orders of magnitude of surface gravity and a representative range of effective temperature. For each star we obtained high S/N TIGRE-HEROS spectra with a spectral resolving power of $R \approx 20,000$ and have measured the Ca II K line-widths of interest, W_0 and W_1 . The main physical parameters are determined by means of iSPEC synthesis and *Gaia* EDR3 parallaxes. Mass estimates are based on matching to evolution models. Using this stellar sample, that is highly uniform in terms of spectral quality and assessment, we derive the best-fit relation between emission line width and gravity g , including a notable dependence on effective temperature T_{eff} , of the form $W_1 \propto g^{-0.229} T_{\text{eff}}^{+2.41}$. This result confirms the physical interpretation of the Wilson-Bappu effect as a line saturation and photon redistribution effect in the chromospheric Ca II column density, under the assumption of hydrostatic equilibrium at the bottom of the chromosphere. While the column density (and so W_1) increases towards lower gravities, the observed temperature dependence is then understood as a simple ionization effect – in cooler stars, Ca II densities decrease in favor of Ca I.

Key words: stars: chromospheres – stars: late-type – stars: activity – stars: fundamental parameters – techniques: spectroscopic

1 INTRODUCTION

Since Eberhard & Schwarzschild (1913), chromospheric emission in the Ca II H&K doublet lines ($\lambda_{\text{H}} = 3968.47 \text{ \AA}$ and $\lambda_{\text{K}} = 3933.68 \text{ \AA}$) is understood to be a universal phenomenon, connected with stellar magnetic activity, and shared by very different kind of late-type stars, which reaches over a wide range of gravities, from Sun to red giants and supergiant stars.

Much of what we know today about chromospheric emission is based on the pioneering work of Olin C. Wilson and his group at the Mount Wilson Observatory, spanning 6 decades of his life. Obviously, strength and width of that emission contains vital information of the chromospheric heating processes and fundamental physical properties of this otherwise elusive atmospheric layer.

One of the most recognized publications of O. C. Wilson’s scientific legacy is his work with M. K. Vainu Bappu of 1957 (Wilson & Bappu 1957), in which an empirical and apparently universal relation was found between the line width $\log W_0$ of the Ca II K chromospheric emission, taken at half-peak intensity, and the stellar absolute visual magnitudes for a sample of 185 late-type stars. Hampered by the lack of precise distances, Wilson (1967) tried to improve this empirical relation. The same lack of precision in giant luminosities, whose parallaxes were too small to be measured directly in those days, made it impossible to test for the dependence on effective temperature and other physical parameters, and to this day it also remains debated, how precise and universal that relation is.

A major factor in the formation of the observed chromospheric emission line profile is the numerous photon absorption and re-emission processes occurring between the bottom of chromosphere, where the emission is produced, and the top, where the observed line profile emerges. In the absence of considerable collision rates for the Ca II H&K transition because of the low chromospheric densities, almost always an absorbed photon is re-emitted. As laid out by Ayres et al. (1975), during this process the photons migrate towards the wings of the line profile function, where their escape probability is greater, since the optical depth there is less.

Consequently, there is a line broadening effect, caused by the large optical depth and saturation at the centers of the Ca II H&K lines, which depends on the column density present in each particular chromosphere. This widening effect is larger for stars with lower gravity, notably giant stars. More luminous giants have a lower gravity, for which hydrostatic equilibrium at the bottom of the chromosphere demands larger scale heights and consequently, a broader Ca II H&K emission.

In particular, the many absorption and re-emission processes that each emerging photon undergoes, is favoring a migration into the wings of the line profile function, which results (as briefly explained above) in the density broadening of the emission line. The simple explanation of this process by Ayres et al. (1975) and Ayres (1979) suggests a clear relation between column density N and gravity g ($N \propto 1/\sqrt{g}$) and yields a dependence of the foot-to-foot emission-line width W_1 with gravity of the order of $W_0 \propto g^{-0.25}$. Comparing giants with known physical parameters, this is essentially consistent with observations (see, e.g. Ayres et al. (1975), Lutz & Pagel (1982), or Park et al. (2013), to name a small selection of work done on

* email: fd.rosasportilla@ugto.mx

this topic). However, in such work, hitherto a 1:1 relation between the two respective line widths W_1 and W_0 has always been implied, simply relying on the idea of homologous emission line profiles.

The other important factor, apart from gravity, in the dependence of emission-line width on physical parameters is the effective temperature T_{eff} , since the ionization balance Ca II:Ca I matters for the Ca II column density as well. Underestimating this term can severely reduce the apparent dependence on gravity, since the giants higher up in the RGB and AGB are not only characterized by a lower gravity but also a lower effective temperature. This establishes cross-talk and the necessity to solve very well for the dependence on *both* these physical stellar parameters. However, the notoriously difficult task to assess T_{eff} with cool giants has hindered exactly all efforts in this regard.

Another complication arises from the effects of strong activity on the chromospheric emission line width, as found with very active binaries (see [Montes et al. \(1994\)](#)). Apparently, the emission line width can be broadened by local plasma motions along magnetic loops. This adds to the above density broadening in the non-active chromosphere and, when not taken into consideration, can offset efforts to find the correct relation of the pure density broadening with the fundamental physical parameters. In this context, it is important to recognize that chromospheric emission increases, by virtue of rising magnetic activity, on the upper AGB ([Schröder et al. 2018](#)). On the other hand, to obtain a precise width measurement, it is desirable to have an emission that exceeds the basal flux. Hence, moderate activity seems acceptable in a suitable stellar sample, but strong activity must be avoided.

This study attempts to be conscious of the above described problems and is an attempt to improve the empirical basis for the physical relation behind the Wilson-Bappu effect. Our motivation is to verify the interpretation of [Ayres et al. \(1975\)](#) as a density broadening effect to a higher level of confidence than previous studies. The alternative suggestion of a Doppler broadening by turbulence (e.g. [Reimers \(1973\)](#), and see extensive discussion in [Lutz & Pagel \(1982\)](#)), seems unlikely already because the inferred turbulent velocities would have to become clearly supersonic in giants and supergiants.

In order to deliver a most precise assessment of the physical relation underlying the Wilson-Bappu effect, we here present a sample of cool stars, covering four orders of magnitude of gravity and a representative range of effective temperatures, for which we obtained high S/N (typically 50-70 at Ca II K), $R \approx 20,000$ TIGRE spectra of a uniform quality across the sample. In addition, we assess the physical parameters uniformly with a consistent method, as described below, using the precise *Gaia* EDR3 parallaxes to minimize spectroscopic analysis ambiguities and cross talk between poorly derived physical parameters. We developed a method, dealing well with the residual noise on the observed emission line profiles, to measure both line widths of interest (W_0 and W_1). Verifying their relation, which is not exactly 1:1, we find this to be an additional, hitherto neglected factor in the comparison of theoretical prediction (using W_1 with observation based on O.C. Wilson's W_0 , which can be measured to higher precision).

2 OBSERVATIONS

2.1 The stellar sample

In order to revise, how the widths of the K emission-line of Ca II behave as a function of (a) the surface gravity $\log g$ and (b) the effective temperature T_{eff} , we selected a sample of 32 well know stars

with spectral types G and K, and luminosity classes I to V. This representative selection covers the large range of $\log g$ from 0.9 to 4.5 dex, while T_{eff} values reach from 3844 to 6013 K (see Table 1). The latter is restricted by the tested reliability of spectroscopic assessment consistency (details are described below).

The state of activity is mostly low to moderate, see the plots of the chromospheric Ca II K emission line profiles in Appendix B. Apart from the aforementioned complications with the emission from very active regions in the chromosphere, we also avoid another problem: the rotational velocities and their variation across the sample remain within the spectral resolution of TIGRE-HEROS (see below), which is equivalent to 7.5 km/s. Only some of the most active giants reach rotation velocities of over 8 km/s, see e.g. [Aurière et al. \(2015\)](#) (Table 3 therein). The same can be said about the turbulent velocities (of the order of several km/s in both, the photosphere and lower chromosphere), which should – by comparison to the widening by the Wilson Bappu effect – not be of much significance.

Included in our sample are the four Hyades K giants, which mark – according to their X-ray and other activity properties, see [Schröder et al. \(2020\)](#) – low to strong solar activity. The other sample stars fall into this range as well. Please note, that (1) the scales in Appendix B are not the same, (2) the photospheric line depths vary a lot, giving large contrast in a cool giant like Arcturus to even the pure basal chromospheric flux, and (3) even the strongest solar activity, in the wider stellar context, is very moderate by comparison.

Thanks to the recently published parallaxes of the *Gaia* EDR3 catalogue ([Gaia Collaboration et al. 2021](#)) of the ESA *Gaia* mission ([Gaia Collaboration et al. 2016](#)) and using reasonable estimates of the stellar mass M_* from evolution tracks that match the luminosity L and T_{eff} of each respective star, derived provisionally by a spectral fitting process, we obtained the parallax-based surface gravities, which in turn help to maximize the non-spectroscopic information on each star. In an iterative approach, we then improved the effective temperature derived for each star from spectral synthesizing by selecting for those least residuals solutions, which reproduce the respective calculated gravity.

Only in four cases, with the three very bright stars α Tau (HD 29139), α Hya (HD 81797) and α Boo (HD 124897), as well as the bright eclipsing binary ζ Aur (HD 32068), *Gaia*'s EDR3 parallaxes are not reliable. In these cases, we used the *Hipparcos* parallaxes ([ESA 1997](#)), instead, since their accuracy is not limited so much for the brightest stars, and for ζ Aur it is in good agreement with the distance obtained from the observed binary system information (see [Schröder et al. \(1997\)](#)).

2.2 Spectroscopic observations with TIGRE

To start with a homogeneous set of spectra of comparable quality, all stars of this sample were observed with the 1.2 m robotic telescope TIGRE ([Schmitt et al. 2014](#)) located near Guanajuato, central Mexico. It is equipped with the HEROS echelle spectrograph, which has a moderately-high uniform resolution of $R \approx 20,000$ over the broad wavelength range from about 3800 to 8800 Å, and produces spectra of good quality – typically S/N ~ 100 or more, averaged over the spectrum, which corresponds to 50-70 in the Ca II H&K line region of a cool star.

The broad wavelength coverage of HEROS is achieved by two separate channels and cameras (for *red* and *blue* light, named channel R and channel B). In this way, the cameras and the cross-dispersers are individually optimized for each wavelength region in sensitivity, the echelle orders well separated, and resolution kept uniform. There is only a small gap of about 120 Å around 5800 Å

(located on the blue side of the sodium D line), caused by the characteristics of the dichromatic beam splitter.

The advantage of TIGRE-HEROS spectra is the versatility of their use. While we obtain information on the chromospheric Ca II H&K emission from the B channel spectra, the R channel spectral range is more suitable to spectral synthesizing and the R camera has the best S/N. Flexible scheduling of the robotic telescope provided us with the required observations, including several takes of each star, over the course of about a year.

To improve our measurements of Ca II K emission-line widths, we typically added two or three spectra of the B channel, following a quality control *by eye* to discard anomalous differences between different takes. With this approach, we avoided the effects of electronic noise or under-exposure in nights of bad transparency, optimize S/N, as well as our measurements of the emission line widths.

3 DERIVING THE PHYSICAL PARAMETERS

3.1 Calculation of parallax-based gravities

In a first step to calculate the parallax-based gravities, we derived absolute visual magnitudes via the *Gaia* EDR3 parallaxes and available photometry, and estimated stellar masses M_* using an approximate preliminary analysis of its position in the Hertzsprung-Russell diagram to find the matching evolution track. We used the photometric apparent magnitudes from the SIMBAD database in the V band (m_V), as well as the color index $B - V$. The parallaxes in milliarcseconds (and distances in parsecs) were taken from the *Gaia* EDR3 archive. We applied the parallax zero-point correction of [Lindgren et al. \(2021\)](#), using their published Python code. No interstellar extinction correction was applied, because the average distance of our sample stars is below ~ 100 pc.

To determine the bolometric magnitudes and, finally, each luminosity, we applied the bolometric corrections (BC) from [Flower \(1996\)](#) for which the effective temperature T_{eff} , or the color index $B - V$, is required. As a start value (to be refined later) for the T_{eff} we used the average of the PASTEL catalogue entries ([Soubiran et al. 2016](#)) for each sample star.

[Flower \(1996\)](#) expresses the bolometric correction in the V -band (BC_V) as a function of the effective temperature of the form: $BC_V = a + b(\log T_{\text{eff}}) + c(\log T_{\text{eff}})^2 + \dots$, for three different temperature ranges. The coefficients a, b, c, \dots are shown in his Table 6 for each interval, but because of a typographical error, the powers of those coefficients were omitted. A fact that was clarified and corrected by [Torres \(2010\)](#). In addition, [Flower \(1996\)](#) calculates $\log T_{\text{eff}}$ as a function of color index of the form $\log T_{\text{eff}} = a + b(B - V) + c(B - V)^2 + \dots$ where the coefficients a, b, c, \dots are taken separately for supergiants or for main sequence stars, subgiants and giants. However, the values of BC_V differ a bit, depending on whether the color index or the effective temperature is used. To have a better approximation and eliminate possible differences, we used the average of the resulting two values of BC_V , derived from $B - V$ and T_{eff} , respectively. Finally, the luminosity in solar units was calculated using the relation $\log L = (4.74 - M_V - BC_V)/2.5$, where we applied a solar visual absolute magnitude of 4.74.

Using the stellar luminosities and effective temperatures, the stars were located in a Hertzsprung-Russell diagram (HRD). The M_* were estimated using a grid of stellar evolution tracks that we computed with the Cambridge (UK) Eggleton code in its updated version ([Pols et al. \(1997\)](#), [Pols et al. \(1998\)](#)), with the quasi-solar metallicity of $Z = 0.02$ (see Fig. 1).

According to the PASTEL catalogue, our sample has an average metallicity of -0.05 dex, i.e. close to solar metallicity. However, taking into account the residual differences, we need to consider that any smaller metallicity makes a star of given mass and age more luminous and less cool, caused by its lower opacities, and the stellar position in the HRD is shifted to the lower left, see e.g. [Schröder et al. \(2013\)](#). Consequently, because of such miss-matches based on the residual differences of the stellar metallicities from solar, we considered an uncertainty for each stellar mass estimate of about 10 percent.

Finally, the surface gravity of each sample star was calculated from the respective stellar luminosity, mass, and (initial) effective temperature as follows. If R_* is the stellar radius, $\log L \propto \log(R_*^2 T_{\text{eff}}^4) \propto \log(M_* g^{-1} T_{\text{eff}}^4)$. Finally, if $\log g_{\odot} = 4.437$ (in units of cgs) is the solar surface gravity, the surface gravity is given by

$$\log g = 4.437 + \log\left(\frac{M_*}{M_{\odot}}\right) - \log\left(\frac{L}{L_{\odot}}\right) + 4\log\left(\frac{T_{\text{eff}}}{T_{\odot}}\right). \quad (1)$$

Using equation 1, this resulted in preliminary gravities for the sample. We used this value to derive the effective temperatures by means of spectral synthesizing (see below), avoiding solutions with wrong gravity and the resulting cross-talk into T_{eff} , see ([Schröder et al. 2021](#)). Then the calculated gravities were updated with these self-determined T_{eff} values. We repeated this procedure to finally refine the effective temperatures as well, where needed. Table 2 summarizes our final results for all 32 stars used in this study.

3.2 Deriving effective temperatures by spectral synthesizing

To derive stellar parameters, T_{eff} in particular from the R channel of TIGRE-HEROS, we used the spectral analysis toolkit iSPEC ([Blanco-Cuaresma et al. 2014b](#)) in its latest Python 3 version (v2020.10.01) ([Blanco-Cuaresma 2019](#)). It allows a comparison of an observed spectrum with synthetic spectra, interpolated from atmospheric models of different physical parameters. The best match, defined by the least differences (χ^2 method) then defines, at least in principle, the corresponding physical parameters. However, in practice there are a number of complications, mostly of physical nature, as pointed out by [Schröder et al. \(2021\)](#). Therefore, information external to the spectroscopic synthesizing is vital to allow testing and to filter seemingly equivalent best-fit solutions.

These problems are mostly caused by a large minimal χ^2 level, produced by the residual mismatches of line strengths (atomic f -values), as well as by subtle, unnoticed blends with other lines – even in a well-selected, representative subset of seemingly reliable lines. Furthermore, any such subset is only representative and usable for a limited range of effective temperatures. In addition, towards the low end of stellar effective temperatures, NLTE effects may be mismatched by the model libraries that iSPEC can use. These complications set limits and require a careful handling of the parameter assessment, applied consistently to all sample stars.

We applied the spectral synthesis process to determine the stellar parameters only in the R-channel of the spectrum, given its better S/N in comparison with the B-channel of HEROS, and its lesser line density, better avoiding line blends interfering with the analysis. We then developed an iSPEC script (iSPAR v4.4.3), written in Python 3, to perform the spectral synthesizing by an algorithm, which uses the very useful iSPEC tools in a consistent manner.

We used the grid of MARCS atmosphere models ([Gustafsson et al. 2008](#)) included in iSPEC. For the reference solar abundances,

we used the values published in [Grevesse et al. \(2007\)](#). The synthetic spectra were calculated using the radiative transfer code TURBOSPECTRUM version 15.1 ([Alvarez & Plez \(1997\)](#), [Plez \(2012\)](#)), which uses already spherical models instead of the plane-parallel approximation (a better approach for giant stars).

When spectral synthesis methods are applied to spectroscopic analysis, parameter determination is complicated by having to fit several of them at the same time, as this approach causes a multitude of ambiguous best-fit solutions. These are caused by the fact that one mismatched parameter can be compensated in its effect by the mismatch of others, named as *cross-talk*, still resulting in a seemingly good representation of the observed spectrum. ISPEC therefore finds different solutions in parameter space, depending on the choice of the initial values, which all need to be explored and tested. We based our algorithm therefore on the considerations of [Schröder et al. \(2021\)](#), who showed a fast method for determining the physical parameters of main sequence stars with moderate resolution spectra, where that was possible. For example, there are no reliable *ubvy*-photometry-derived metallicity values available for giant stars. Still, our script aims on minimizing cross-talk by maximizing the use of non-spectroscopic information to filter out those best-fit solutions with parameters contradicting that information external to the synthesizing process.

A very delicate procedure preceding the synthesizing step is the fit of the pseudo-continuum of the observed stellar spectrum in question and the line selection for the synthesizing procedure with ISPEC. After several comparative tests, we found that the impact of this step on the final results of the stellar parameters is not negligible, since it affects the χ^2 sums and their minima in parameter space. We explain in detail the pseudo-continuum adjustment and the line selection in the appendix A. The latter is important for the successful spectroscopic synthesizing and is a compromise between completeness and quantity versus line data quality.

3.2.1 Final stellar parameter determination

For the final analysis of the now readjusted, normalized observed spectrum by parameter synthesizing, we set the start values to the averages of T_{eff} and $[M/H]$ in the PASTEL catalogue, while the initial gravities were calculated using equation 1. Initial v_{mic} values – as detailed in the appendix A for the synthetic spectra used to guide the continuum readjustment – are set to the velocities used for the PHOENIX library ([Husser et al. 2013](#)), while v_{mac} is set again by equation A1.

The best-fit results of ISPEC synthesizing are sensitive to the choice of the initial parameters. The further exploration of the parameter space therefore follows the strategy of [Blanco-Cuaresma et al. \(2014b\)](#), varying the initial values in steps. Our ISPEC script implements an analysis that varies the initial parameters by as much as follows: ± 100 K for T_{eff} , ± 0.15 dex for $\log g$, and ± 0.15 dex for $[M/H]$, each time repeating the process for a total of 27 calculations around the initial values. Then stellar parameters with the best χ^2 result of all solutions is chosen. These step-sizes and the following sequence performed best in our tests described in subsection 3.4.

Based on the strategy of [Schröder et al. \(2021\)](#), the best way to determine the stellar parameters is to leave only one of them free at a time, while the others remain fixed, going through the following sequence in a partially iterative procedure: (1) refine v_{mic} ; (2) having re-set v_{mac} through equation A1, based on the now refined v_{mic} , refine gravity ($\log g$); (3) now refine $v \sin i$; (4) refine T_{eff} , $[M/H]$ and $[\alpha/\text{Fe}]$; (5) refine v_{mac} ; (6) refine again v_{mic} ; (7) refine again T_{eff} , $[M/H]$ and $[\alpha/\text{Fe}]$; (8) refine again $v \sin i$ and finally, (9) refine again

$[\text{Fe}/H]$. However, with the resolution of TIGRE-HEROS spectra in mind, we are aware that different turbulence and rotation velocity values under 3 km/s bear no physical meaning, considering our modest spectral resolution. Still, there is a need to adjust them in a tested way to minimize cross talk (see below). We should also note, for the complications with cross-talk in combination with the limited spectral resolution, that we do not consider the rotation and turbulence velocity values derived here of any credibility because they are typically half the instrumental line profile width. Our tests only demonstrate the reliability of the main physical parameters, namely effective temperature, gravity, and metallicity.

3.3 Consistency check with parallax-based gravities

The improved values of T_{eff} obtained from spectral synthesis with our ISPEC script give slightly different positions in the HR diagram. We therefore repeated, at this point, the mass estimates and, consequently, recalculated the parallax-based gravities (in the same way as in subsection 3.1), and finally also repeated all synthesizing steps of above. Table 1 summarizes the final stellar parameters obtained for the sample stars with this method, while Table 2 details the distances, magnitudes, physical parameters and parallax-based gravities. Fig. 1 pictures the final estimation of the masses for the stellar sample on a grid of stellar evolution tracks, computed with the Cambridge (UK) Eggleton code for solar metallicity.

To ensure that our assessment of the stellar parameters of the sample is sufficiently reliable, we tested our results as follows: Fig. 2 and Fig. 4 show a comparison between our results for T_{eff} and $[\text{Fe}/H]$ by spectral synthesis (as described above) and the average values in the PASTEL catalogue. Fig. 3 shows a comparison between our results for $\log g$ by spectral synthesis and the parallax-based gravities of Table 2. The blue line in these graphs represents the ideal of a 1:1 relation; the uncertainties of our estimations were calculated as explained in subsection 3.4.

3.4 Test with Gaia FGK Benchmark Stars

The *Gaia* FGK Benchmark Stars (GBS onwards, [Jofré et al. \(2014\)](#), [Blanco-Cuaresma et al. \(2014a\)](#), [Heiter et al. \(2015\)](#), [Jofré et al. \(2015\)](#), [Hawkins et al. \(2016\)](#), [Jofré et al. \(2017\)](#)) is a high resolution and high S/N library of a set of calibration star spectra. This library constitutes a set of very well-known stars especially convenient for spectral analysis assessments. It covers a wide range in effective temperature (3500 to 6600 K), surface gravity (0.50 to 4.60 dex) and metallicity (-2.70 to 0.30 dex). In addition, the stellar parameters of the set was mainly obtained from methods independent of spectroscopy.

We used four well-know stars from the GBS, δ Eri (HD23249), α Tau (HD 29139), *Arcturus* (HD 124897) and the *Sun*, to test the reliability of our method, as well as to see, if the use of TIGRE-HEROS spectra might somehow affect our results for reasons based on any instrumental issues. Therefore, spectra of three different resolutions and S/N (see [Blanco-Cuaresma et al. \(2014a\)](#) and references therein) are tested with our script and line list, after downgrading their resolution to the one of TIGRE-HEROS, $R = 20,000$. The spectra in the GBS cover a wavelength range from 4800 Å to 6800 Å. For a meaningful comparison, we cut both GBS and R-channel TIGRE-HEROS spectra down to the same range of 5800 Å to 6800 Å.

The tests allow us to prove the reliability of our ISPEC script on spectra other than TIGRE-HEROS, as well as the use of our line list in Table A1. We performed tests for many scenarios, including

Table 1. Stellar parameters derived with our iSPEC script.

Star	Type ^a	T_{eff}^b [K]	$\log g^c$ [dex]	[M/H] [dex]	[α /Fe] [dex]	v_{mic}^d [km/s]	v_{mac}^d [km/s]	$v \sin i^d$ [km/s]	[Fe/H] [dex]
HD 8512	K0IIIb	4762 (17)	2.50 (0.04)	-0.15 (0.01)	0.04 (0.02)	1.66	3.44	0.00	-0.15 (0.01)
HD 10476	K1V	5174 (24)	4.50 (0.02)	-0.10 (0.02)	0.01 (0.02)	0.96	0.00	0.00	-0.10 (0.02)
HD 18925	G9III	5032 (26)	2.30 (0.00)	-0.17 (0.02)	-0.04 (0.03)	1.39	3.67	1.20	-0.16 (0.01)
HD 20630	G5V	5678 (43)	4.56 (0.05)	-0.03 (0.04)	0.01 (0.04)	1.31	3.70	0.60	-0.02 (0.02)
HD 23249	K0+IV	5032 (28)	3.70 (0.06)	0.03 (0.02)	0.02 (0.03)	1.18	0.48	0.00	0.00 (0.02)
HD 26630	G0Ib	5572 (31)	1.90 (0.11)	0.01 (0.02)	0.02 (0.03)	3.25	5.79	9.98	0.01 (0.02)
HD 27371	G9.5IIIab	4988 (31)	2.93 (0.06)	0.10 (0.03)	-0.10 (0.03)	1.58	3.22	0.00	0.07 (0.02)
HD 27697	G9.5III	4989 (32)	2.68 (0.06)	0.12 (0.03)	-0.03 (0.03)	1.58	3.78	0.00	0.09 (0.02)
HD 28305	G9.5III	4950 (25)	2.79 (0.07)	0.18 (0.02)	-0.12 (0.03)	1.65	2.51	0.00	0.14 (0.02)
HD 28307	G9III	5009 (28)	2.96 (0.04)	0.14 (0.02)	-0.09 (0.03)	1.67	2.46	0.00	0.12 (0.02)
HD 29139	K5+III	3844 (18)	1.30 (0.04)	-0.19 (0.01)	-0.14 (0.02)	1.65	3.07	3.94	-0.22 (0.02)
HD 31398	K3II-III	4077 (13)	1.34 (0.03)	-0.07 (0.01)	-0.17 (0.01)	2.11	4.02	3.93	-0.09 (0.01)
HD 31910	G1Ib	5665 (26)	1.91 (0.11)	-0.04 (0.02)	0.05 (0.03)	3.79	7.78	10.66	-0.02 (0.01)
HD 32068	K5II	3980 (18)	1.21 (0.03)	-0.05 (0.01)	-0.17 (0.02)	1.86	2.84	6.35	-0.06 (0.01)
HD 48329	G8Ib	4591 (11)	1.38 (0.03)	0.05 (0.01)	-0.13 (0.01)	2.93	5.37	9.08	0.03 (0.01)
HD 71369	G5III	5266 (27)	2.74 (0.07)	-0.11 (0.02)	0.05 (0.03)	1.76	4.32	0.00	-0.10 (0.02)
HD 81797	K3IIIa	4117 (18)	1.57 (0.03)	-0.08 (0.01)	-0.15 (0.02)	1.89	3.31	1.67	-0.09 (0.01)
HD 82210	G5III-IV	5342 (58)	3.42 (0.15)	-0.30 (0.05)	0.03 (0.05)	1.69	5.40	0.00	-0.30 (0.03)
HD 96833	K1III	4630 (23)	2.14 (0.06)	-0.10 (0.02)	0.03 (0.03)	1.65	3.41	0.00	-0.11 (0.02)
HD 104979	G8III	4990 (30)	2.69 (0.08)	-0.33 (0.03)	0.05 (0.03)	1.43	0.98	0.00	-0.34 (0.02)
HD 109379	G5IIB	5325 (28)	2.63 (0.06)	0.14 (0.02)	0.01 (0.03)	1.51	2.78	5.90	0.14 (0.02)
HD 114710	F9.5V	6013 (52)	4.37 (0.06)	0.01 (0.04)	0.01 (0.03)	1.12	1.94	3.37	0.02 (0.02)
HD 115659	G8IIIa	5127 (30)	2.94 (0.05)	0.03 (0.03)	-0.04 (0.03)	1.57	3.96	0.46	0.02 (0.02)
HD 124897	K1.5III	4339 (18)	1.54 (0.04)	-0.55 (0.02)	0.20 (0.03)	1.75	2.86	0.00	-0.57 (0.02)
HD 148387	G8-IIIab	5079 (36)	2.80 (0.08)	-0.07 (0.03)	0.04 (0.04)	1.53	1.70	0.00	-0.08 (0.02)
HD 159181	G2Ib-IIa	5390 (33)	2.14 (0.10)	0.02 (0.03)	-0.01 (0.03)	2.72	8.22	7.26	0.03 (0.02)
HD 164058	K5III	3965 (14)	1.62 (0.02)	-0.01 (0.01)	-0.16 (0.01)	1.70	3.29	2.62	-0.05 (0.01)
HD 186791	K3II	4074 (15)	1.15 (0.03)	-0.11 (0.01)	-0.15 (0.02)	2.03	3.61	3.52	-0.12 (0.01)
HD 198149	K0IV	5003 (29)	3.30 (0.06)	-0.21 (0.02)	-0.01 (0.03)	1.21	3.05	1.47	-0.22 (0.02)
HD 204867	G0Ib	5604 (27)	1.61 (0.07)	0.02 (0.02)	0.04 (0.03)	2.96	3.34	10.87	0.04 (0.01)
HD 205435	G8III	5118 (33)	2.99 (0.01)	-0.14 (0.03)	0.05 (0.04)	1.77	2.18	0.00	-0.14 (0.02)
HD 209750	G2Ib	5432 (19)	1.91 (0.08)	0.08 (0.02)	0.01 (0.02)	3.14	6.70	9.79	0.09 (0.01)

^a Spectral type from SIMBAD database.^b The nominal and very small error on T_{eff} reported by iSPEC does not enter our uncertainty of parallax-based gravities. We rather apply a more realistic uncertainty of ± 100 K according to our tests in subsection 3.4.^c The surface gravity values derived by iSPEC won't be used in our analysis, we show them only as a reference to the consistency achieved.^d Because of our modest spectral resolution ($R \approx 20,000$), turbulences and rotation velocities derived of 3 km/s are not physically meaningful. Nevertheless, the average nominal error reported by iSPEC is ~ 0.5 km/s.

different resolutions, added spectra or using just one, automatic determination of parameters, varying the initial parameters, different wavelength ranges, etc. However, for the purpose of this publication, we only present the results of the first two tests, since the other test results do not differ much.

Table 3 summarizes the test results for T_{eff} , $\log g$, and [Fe/H], comparing the outcome of our iSPEC script for different resolutions. To test for any changes in the stellar parameter determination, whether we add or not several TIGRE-HEROS spectra, we used three spectra for each star with an average S/N ≥ 100 .

These tests prove the reliability and robustness of the physical parameters obtained from the spectral synthesis approach taken with our iSPEC script, employed on different resolutions. Therefore, we consider the total uncertainty of stellar parameters with this method as: $T_{\text{eff}} = \pm 100$ K, $\log g = \pm 0.15$ dex and [Fe/H] = ± 0.15 .

4 THE CA II EMISSION LINE WIDTHS OF INTEREST AND THEIR MEASUREMENTS

4.1 Formation of the Ca II K emission line and where to take its width

The very cores of the Ca II H&K lines are of such huge optical depth, that they provide one of very few windows into the chromospheres of cool stars. While most line cores in the optical spectrum reflect the physical conditions of the upper photosphere, the Ca II doublet allows us to trace the temperature structure beyond its minimum at the base of the chromosphere, well into the rise, which is manifested by the Ca II H&K line core reversals into emission. An early, extensive review of the chromospheric physics learned from this doublet was given by [Linsky & Avrett \(1970\)](#), and recent reviews are by [Linsky \(2017\)](#) and [Ayres \(2019\)](#). The focus is usually on the K line, often omitting its twin, in order to avoid any confusion which may arise from the overlap of the Ca II H line with the hydrogen H $_{\epsilon}$ line.

Since Ca II is more easily ionized than Mg II and hydrogen, its formation does not reach into the increasingly warmer, uppermost chro-

Table 2. Distances, magnitudes, physical parameters and parallax-based gravities.

Star	D [pc]	$B - V$ [mag]	V [mag]	BC [mag]	$\log(L/L_{\odot})$ [dex]	M_{\star} [M_{\odot}]	$\log g^b$ [dex]
HD 8512	34.48 (0.26)	1.06 (0.05)	0.902 (0.026)	-0.439 (0.059)	1.707 (0.034)	1.70 (0.17)	2.63 (0.11)
HD 10476	7.65 (0.01)	0.84 (0.03)	5.823 (0.013)	-0.235 (0.031)	-0.343 (0.017)	0.85 (0.09)	4.52 (0.09)
HD 18925	70.98 (3.85)	0.70 (0.26)	-1.326 (0.128)	-0.208 (0.112)	2.505 (0.096)	3.90 (0.39)	2.28 (0.17)
HD 20630	9.27 (0.02)	0.67 (0.07)	5.014 (0.054)	-0.101 (0.033)	-0.073 (0.035)	1.00 (0.10)	4.48 (0.11)
HD 23249	9.09 (0.02)	0.92 (0.03)	3.747 (0.014)	-0.287 (0.041)	0.508 (0.022)	1.20 (0.12)	3.77 (0.10)
HD 26630	256.12 (17.25)	0.96 (0.31)	-2.882 (0.156)	-0.201 (0.153)	3.125 (0.124)	5.50 (0.55)	1.99 (0.20)
HD 27371	46.23 (0.39)	0.99 (0.06)	0.325 (0.028)	-0.331 (0.065)	1.894 (0.037)	2.62 (0.26)	2.71 (0.12)
HD 27697	49.32 (0.55)	0.98 (0.07)	0.295 (0.034)	-0.324 (0.072)	1.904 (0.043)	2.75 (0.28)	2.72 (0.12)
HD 28305	44.79 (0.34)	1.01 (0.09)	0.274 (0.067)	-0.354 (0.082)	1.924 (0.059)	2.75 (0.28)	2.69 (0.14)
HD 28307	40.42 (0.71)	0.94 (0.09)	0.807 (0.047)	-0.294 (0.087)	1.687 (0.054)	2.42 (0.24)	2.89 (0.13)
HD 29139 ^a	20.43 (0.32)	1.54 (0.09)	-0.692 (0.044)	-1.333 (0.257)	2.702 (0.120)	1.50 (0.15)	1.21 (0.21)
HD 31398	138.62 (7.27)	1.53 (0.25)	-3.019 (0.124)	-1.128 (0.481)	3.551 (0.242)	6.50 (0.65)	1.10 (0.33)
HD 31910	259.88 (10.86)	0.93 (0.20)	-3.054 (0.101)	-0.177 (0.096)	3.184 (0.079)	5.20 (0.52)	1.94 (0.15)
HD 32068 ^a	240.96 (16.84)	1.22 (0.32)	-3.160 (0.162)	-0.844 (0.285)	3.494 (0.179)	5.10 (0.51)	1.04 (0.26)
HD 48329	269.47 (13.10)	1.41 (0.23)	-4.173 (0.116)	-0.708 (0.267)	3.844 (0.153)	8.20 (0.82)	1.11 (0.23)
HD 71369	55.85 (0.45)	0.85 (0.06)	-0.315 (0.028)	-0.223 (0.042)	2.107 (0.028)	3.20 (0.32)	2.68 (0.10)
HD 81797 ^a	55.28 (0.55)	1.45 (0.06)	-1.743 (0.032)	-0.994 (0.129)	2.987 (0.064)	3.20 (0.32)	1.37 (0.15)
HD 82210	32.13 (0.12)	0.77 (0.04)	2.036 (0.018)	-0.179 (0.030)	1.149 (0.019)	1.70 (0.17)	3.38 (0.10)
HD 96833	43.11 (0.47)	1.14 (0.07)	-0.163 (0.033)	-0.526 (0.074)	2.168 (0.043)	2.40 (0.24)	2.27 (0.12)
HD 104979	51.40 (0.44)	0.99 (0.06)	0.565 (0.028)	-0.330 (0.066)	1.798 (0.038)	2.30 (0.23)	2.75 (0.12)
HD 109379	45.51 (0.48)	0.88 (0.07)	-0.651 (0.033)	-0.227 (0.046)	2.243 (0.032)	3.30 (0.33)	2.57 (0.11)
HD 114710	9.20 (0.01)	0.59 (0.07)	4.431 (0.053)	-0.049 (0.026)	0.139 (0.032)	1.10 (0.11)	4.41 (0.10)
HD 115659	39.22 (0.42)	0.92 (0.07)	0.033 (0.033)	-0.268 (0.064)	1.986 (0.039)	2.90 (0.29)	2.71 (0.12)
HD 124897 ^a	11.26 (0.06)	1.23 (0.04)	-0.308 (0.022)	-0.692 (0.071)	2.292 (0.037)	1.40 (0.28)	1.80 (0.16)
HD 148387	28.01 (0.22)	0.91 (0.05)	0.503 (0.027)	-0.284 (0.043)	1.804 (0.028)	2.55 (0.26)	2.82 (0.11)
HD 159181	119.87 (1.55)	0.98 (0.08)	-2.584 (0.038)	-0.233 (0.052)	3.019 (0.036)	5.00 (0.50)	2.00 (0.11)
HD 164058	46.31 (0.03)	1.53 (0.02)	-1.099 (0.008)	-1.210 (0.113)	2.815 (0.049)	4.10 (0.41)	1.58 (0.14)
HD 186791	179.93 (12.43)	1.51 (0.32)	-3.556 (0.160)	-1.099 (0.541)	3.754 (0.280)	8.00 (0.80)	0.98 (0.37)
HD 198149	14.37 (0.03)	0.91 (0.02)	2.622 (0.011)	-0.289 (0.040)	0.959 (0.020)	1.40 (0.14)	3.38 (0.10)
HD 204867	168.47 (6.02)	0.82 (0.18)	-3.243 (0.088)	-0.143 (0.069)	3.246 (0.063)	5.60 (0.56)	1.89 (0.14)
HD 205435	38.59 (0.15)	0.89 (0.04)	1.087 (0.019)	-0.267 (0.037)	1.564 (0.022)	2.20 (0.22)	3.01 (0.10)
HD 209750	203.54 (17.57)	0.96 (0.39)	-3.603 (0.197)	-0.218 (0.191)	3.420 (0.155)	6.30 (0.63)	1.71 (0.23)

^a Distance calculated using the *Hipparcos* parallaxes (ESA 1997)^b The surface gravity was calculated using Equation 1.**Table 3.** Comparison tests with *Gaia* FGK Benchmark Stars. The original resolution of spectra has been downgraded to $R = 20,000$.

Star	Instrument	Resolution	Add ^a	T_{eff} [K]	ΔT_{eff}^b [K]	$\log g$ [dex]	$\Delta \log g^b$ [dex]	[Fe/H] [dex]	$\Delta[\text{Fe}/\text{H}]^b$ dex
δ Eri (HD 23249)	TIGRE-HEROS	20524	False	4969 (29)	15	3.60 (0.04)	-0.16	-0.01 (0.02)	-0.07
δ Eri (HD 23249)	TIGRE-HEROS	20524	True	4974 (25)	20	3.59 (0.03)	-0.17	0.00 (0.01)	-0.06
δ Eri (HD 23249)	UVES.POP	85000	False	4972 (7)	18	3.64 (0.01)	-0.12	0.05 (0.01)	-0.01
δ Eri (HD 23249)	HARPS	115000	False	4971 (7)	17	3.62 (0.01)	-0.14	0.04 (0.00)	-0.02
α Tau (HD 29139)	TIGRE-HEROS	20366	False	3805 (20)	-122	1.13 (0.03)	0.02	-0.36 (0.02)	0.01
α Tau (HD 29139)	TIGRE-HEROS	20366	True	3798 (16)	-129	1.16 (0.03)	0.05	-0.37 (0.01)	0.00
α Tau (HD 29140)	NARVAL	80000	False	3821 (8)	-106	1.25 (0.02)	0.14	-0.27 (0.01)	0.10
α Tau (HD 29141)	HARPS	115000	False	3838 (17)	-89	1.24 (0.03)	0.13	-0.30 (0.01)	0.07
Arcturus (HD 124897)	TIGRE-HEROS	20435	False	4341 (19)	55	1.60 (0.05)	-0.04	-0.57 (0.02)	-0.04
Arcturus (HD 124897)	TIGRE-HEROS	20435	True	4342 (15)	56	1.61 (0.04)	-0.03	-0.57 (0.02)	-0.04
Arcturus (HD 124897)	UVES.POP	80000	False	4338 (3)	52	1.67 (0.01)	0.03	-0.52 (0.00)	0.01
Arcturus (HD 124897)	HARPS	115000	False	4334 (5)	48	1.64 (0.02)	0.00	-0.50 (0.01)	0.03
Sun	TIGRE-HEROS	20501	False	5750 (41)	-22	4.43 (0.06)	-0.01	-0.05 (0.02)	-0.05
Sun	TIGRE-HEROS	20501	True	5743 (34)	-29	4.43 (0.04)	-0.01	-0.05 (0.01)	-0.05
Sun	UVES	78000	False	5758 (14)	-14	4.45 (0.02)	0.01	-0.03 (0.01)	-0.03
Sun	HARPS	115000	False	5756 (12)	-16	4.44 (0.01)	0.00	-0.02 (0.01)	-0.02

^a Adding three TIGRE-HEROS spectra.^b Differences with values in *Gaia* FGK Benchmark Stars library.

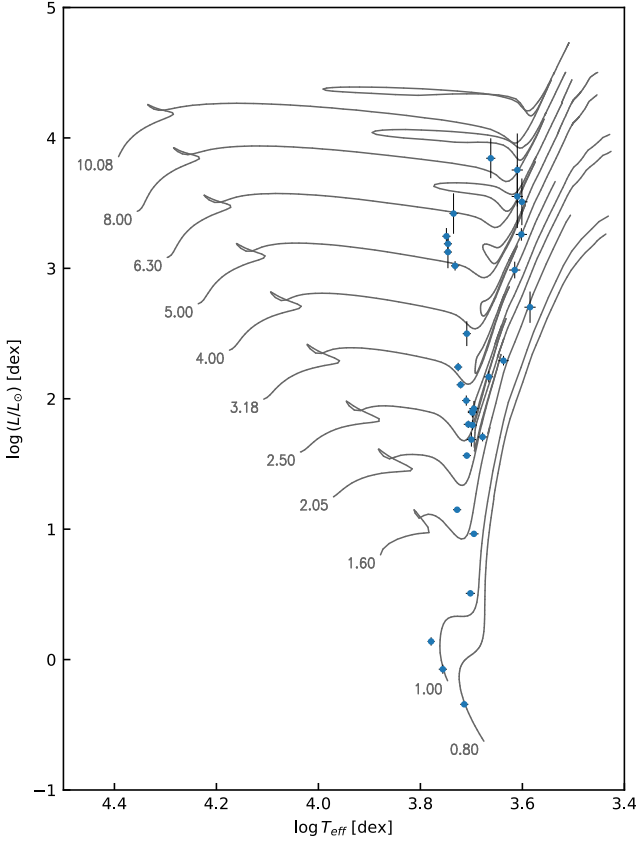


Figure 1. Grid of evolution tracks with solar metallicity for different stellar masses in solar mass units. The grid was calculated using the Cambridge (UK) Eggleton code in its version described and tested by Pols et al. (1997) and Pols et al. (1998).

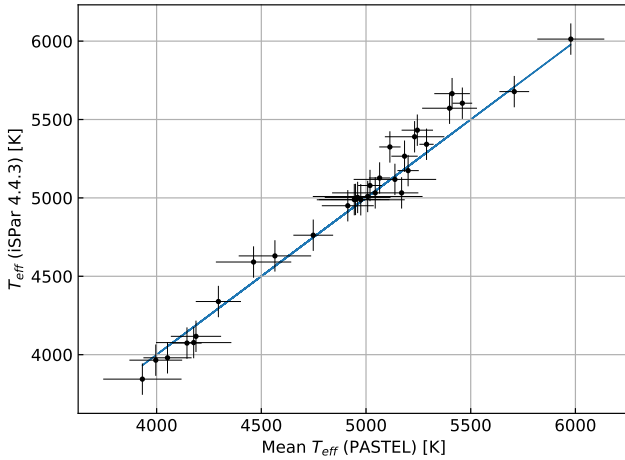


Figure 2. Temperature comparison between the values calculated by spectral synthesis using our ISPEC script and the average values in the PASTEL catalogue.

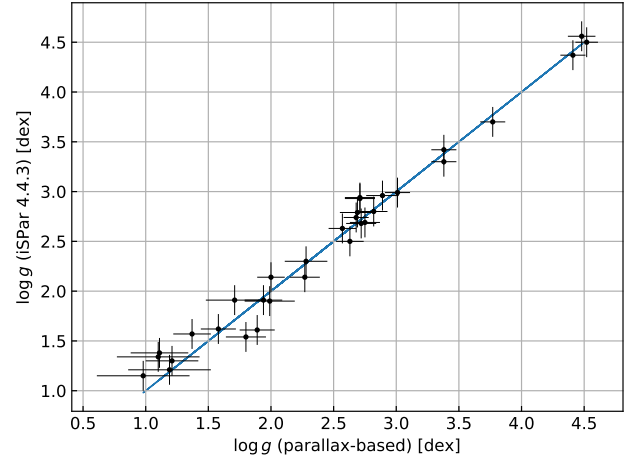


Figure 3. Surface gravity comparison between the values calculated by spectral synthesis using our ISPEC script and the parallax-based gravities using the equation 1.

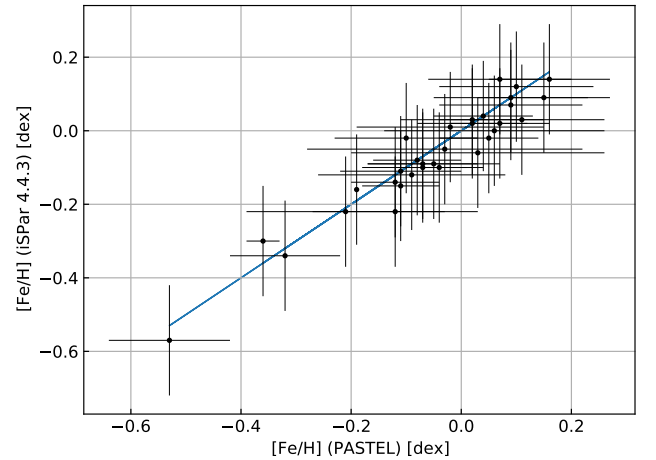


Figure 4. Metallicity comparison between the values calculated by spectral synthesis using our ISPEC script and the average values in the PASTEL catalogue.

mosphere. There, magnetically dominated phenomena like prominences make the interpretation of, for example, H_{α} much more difficult. The K-lines reversal, its K2 emission, further shows a self-reversal (K3), which however must not be interpreted in terms of a temperature profile. Rather, this reversal is the product of extreme NLTE photon line scattering and geometrical distribution in the higher chromospheric layers – therefore much more prominent in luminous giants with their larger chromospheric extent. Hence, for a physical understanding of the lower chromosphere, our interest must be aimed on the outer proportions of the K2 chromospheric emission profile.

Consequently, Wilson & Bappu (1957) based their empirical relation between the chromospheric Ca II K emission line width and visual absolute magnitude M_V on their measurements of W_0 – chosen simply for the benefit of the best measurement precision, when taken as the positions of the outer edges of the calcium emission features.

This is particularly true for measurements on photographic plates, as used in those days. Using the same spectrograms of [Wilson & Bappu \(1957\)](#), [Lutz \(1970\)](#) finally shows that the width at half intensity of the K emission line peak of Ca II is better correlated with M_V unlike the original method used by [Wilson & Bappu \(1957\)](#). Those peaks are also known as K2. Dealing with noisy spectra, the half-peak points are relatively well defined on the steep flanks of even a noisy emission line.

By contrast, the foot-points of the broad photospheric absorption line (K1) to either side of the chromospheric emission are not so well defined, especially in a noisy spectrum, because the deepest point in a shallow depression is ambiguous. But these K1 points are of theoretical significance: They are formed right at the base of the chromosphere, in the temperature-minimum. Assuming the source function there is still dominated by the Planck function, the minimal spectral flux observed in these deepest points of the K line on either side of the chromospheric emission reveals the physical conditions in temperature minimum.

However, as pointed out and illustrated by [Shine et al. \(1975\)](#) (see their Fig. 1), the exact distance and depths of these K1 points depends a lot on partial redistribution (PRD) effects on the K2 wings – becoming considerable, given the large number of photon line scattering events in this strong line prior to each escaping photon. PRD effects further increase with the larger chromospheric column densities in the more luminous giants. In that respect, [Shine et al. \(1975\)](#) already made it clear, that not considering PRD can lead to significant underestimates of the temperature in the temperature-minimum. Likewise, we conclude from their Fig. 1 that PRD and stellar gravity impact on the relation between W_0 , O.C. Wilson’s half-maximum width, and the distance between the K1 points of the chromospheric emission line profile, hereafter referred to as W_1 .

In their layout of a density-broadening explanation of the Wilson-Bappu effect – by the very numerous chromospheric absorption and re-emission events preceding each photon reaching the observer – [Ayres et al. \(1975\)](#) refer to the emission line width as taken between these two K1 foot points (i.e., W_1), simply for its significance by characterizing the base of the chromosphere. In assuming (without saying), as a first-order approximation, homologous emission line profiles across the giant branch, their explanation of the Wilson-Bappu effect, based on the theoretical arguments involving W_1 , is implied to be true for O.C. Wilson’s W_0 as well.

However this simplification is not entirely true, as the theoretical work of [Shine et al. \(1975\)](#) already predicted, and as our measurements confirm below. In particular, when looking at lower gravities, W_1 starts to grow a bit faster than W_0 . Because we are seeking a more precise comparison of theory with observation, this detail needs to be considered as well – which to our knowledge was never done before. The reason for that may simply stem from the difficulty to measure W_1 . Hence, we here present our method to determine well both these line widths, handling well the presence of noise on the observed emission line profile, and used them here consistently for the whole sample.

4.2 Measuring the widths of the chromospheric Ca II K emission line

The best way to use all information in an observed line profile with noise, is to empirically represent the whole profile by a best-fit analytical function, and then derive key quantities from that function. This approach avoids dependence on local noise effects, a particular advantage for measuring the shallow K1 minima by the foot points

of the chromospheric emission, defining W_1 – provided, the representative function covers them well, too.

The physical features of the K emission line of Ca II, however, are difficult to match by the types of profiles mostly used elsewhere in the analysis of spectral lines: Gaussian, Lorentzian, or a convolution of both, called *Voigt* profile. [Lutz \(1970\)](#) shows for the simplest case of a Ca II K emission line, which does not have central self-absorption, that even there fitting a Lorentzian profile does not match correctly neither the *wings* of the line, nor the region of the *peak*. On the other hand, while a Gaussian fit matches better the line wings, it cannot represent the peak area either, because it is wider than the wing-matching Gaussian function. To fully consider the additional complexity of chromospheric Ca II emission line profiles with central self-absorption, as required by this work, none of those three profiles are remotely adequate, and their use would only result in totally incorrect line width measurements.

To measure the width of the K emission line of Ca II in the spectra of our stellar sample, we wrote a dedicated code, HALF-INTENSITY EMISSION WIDTH (HIEW v4.0), developed in C++. Our script HIEW works along a routine, which involves five main stages: (1) reading the configuration file and spectrum; (2) K-line representation by cubic splines to reduce variations caused by electronic noise in the spectrum; (3) determination of the minima and maxima in each of *blue* B and *red* R peaks of the K-line profile; (4) determination of the half peak intensity level, based on the average of the B and R peak intensity; (5) calculation of W_0 as the half-intensity emission width, and W_1 as the foot point separation of the representative emission line profile spline function.

In the observed spectrum, the real emission line profile is folded with the instrumental profile, and in this way the observed line is broadened by the limited spectral resolution. The instrumental profile width of TIGRE-HEROS is a function of wavelength and the instrumental FWHM in the Ca II K line region is $\sim 0.19 \text{ \AA}$ ([Schmitt et al. \(2014\)](#), [Czesla \(2014\)](#)). However, the way of correction of the measured K-line widths by the instrumental profile width is a delicate matter, and has been discussed in detail already by [Lutz \(1970\)](#).

To consider in more detail the effects of the TIGRE-HEROS resolution in our measurements, we simulated an emission K line-profile using, as a first approximation, a sum of analytical functions (Gaussian, Voigt and both) even when, as [Lutz \(1970\)](#) clearly showed, the complexity of chromospheric Ca II emission line profiles does not adequately fit any of these analytic functions. However, our tests showed that the use of two Gaussian functions – with positive amplitude to fit the emission (K2) and negative amplitude to fit the autoabsorption (K3) – appears to match sufficiently well a number of representative cases of observed emission K line-profiles of our sample.

In a first step, we normalized the observed emission line by a cubic spline fitting of the Ca II absorption. Then, we convoluted a simulated profile with the instrumental line profile (ILP) of TIGRE-HEROS and, by an RMS criterion, we improved recursively the analytical parameters of the functions considered. After 30 iterations the convolution of the simulated profile converges with the observed line profile. Fig. 5 shows the effect of the TIGRE-HEROS resolution in a simulated emission line for HD 205435 and the comparison with a observed Ca II K emission line. As we could have expected, the maximum, and half maximum points of the simulated and observed line profiles differ. Nevertheless, the difference of W_0 line widths for both K line-profiles are within the instrumental error ($\sim 0.11 \text{ \AA}$, equivalent to the standard deviation of TIGRE-HEROS’ instrumental line-profile close to the K-line of Ca II).

The two extremes, to subtract the instrumental resolution linearly,

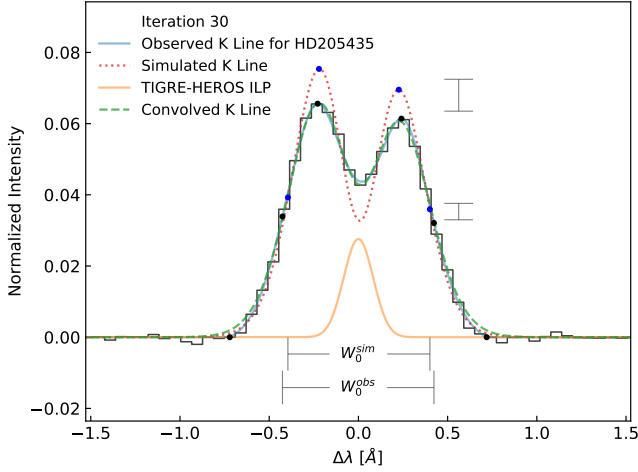


Figure 5. Simulation of the normalized Ca II K emission line for HD 205435. We used a sum of two gaussian functions to simulated a K line profile (dotted red line) without the effect of the instrumental line profile of TIGRE-HEROS (solid orange line). The convolution between the simulated K emission line and instrumental line profile (dashed green line) fits well enough to the observed K emission line for HD 205435. Points mark the minimum, maximum, and half-maximum of the simulated (blue dots) and observed (black dots) line profiles. In the right part, we show the differences of the maximum averages and half-maximum averages. In the bottom part, we show the W_0 for simulated and observed emission line.

or in quadrature, are correct only if either both the instrumental profile and the line profile are lorentzian functions, or in the latter case, gaussians. But the K2 emission line shape is clearly neither, as mentioned above, and in the case of the HEROS spectrograph, the line profile is not gaussian (see Czesla (2014)). If anything, then the economic coverage of the nominal spectrograph resolution by only three pixels and the scattering characteristics in the fiber-feed may enhance the wings of the effective instrumental profile and bring it closer to a lorentzian function.

As already studied by Lutz (1970), the choice of this correction does matter a little bit, as it systematically affects the narrower lines more. We tested both approaches and find a maximum difference of 0.02 in the gravity exponent. In addition, the difference of widths of simulated, linear and quadrature subtraction are within the instrumental error of TIGRE-HEROS. However, given the analysis above, neither case is *a priori* a choice more justifiable than the other. Interestingly, O. C. Wilson always used the simple linear subtraction, and the detailed revision of his measurements by Lutz (1970) showed that it seemed to be more consistent than a trial with a subtraction in quadrature. Apparently, and by coincidence, another detail of the measuring process comes in to compensate any theoretical offset: washed-out (by limited resolution) narrower lines tend to be measured, effectively, further down than broad lines, when aiming at the 50 per cent level of the observed (and so broadened) profile. Hence, we settled for the simple linear correction method to arrive at our *true* widths of the Ca II K emission line. The appendix B contains the line width measurements, and Table 4 summarizes these results for the whole stellar sample.

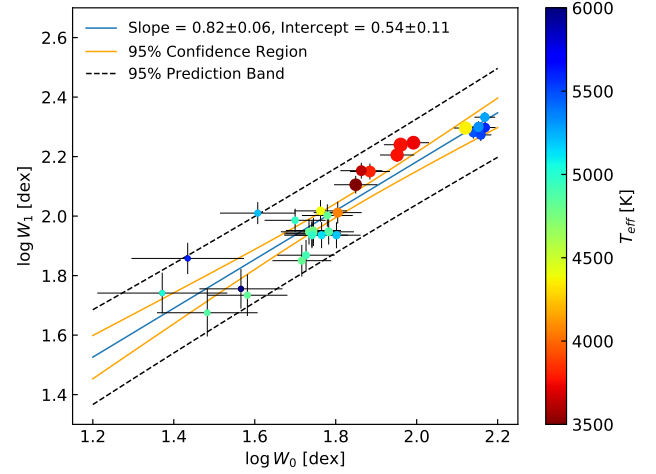


Figure 6. Comparison of line width measurements $\log W_1$ vs $\log W_0$ of the Ca II K emission line for the stellar sample. We used the logarithmic values of widths in km/s. The blue line corresponds to a linear fit. The color code represents the effective temperature, and the point-size represents the surface gravity with larger points for lower gravities.

4.3 Are W_0 and W_1 analogous measurements of the Ca II K emission line width?

As pointed out before, Ayres et al. (1975) and also Cram & Ulmschneider (1978) compared and proposed empirical width-luminosity correlations, referring to the Ca II K₁ minimum features, which means the W_1 widths, not O.C. Wilson's W_0 . However, in his work Ayres (1979) argues that W_0 should be, much like W_1 , proportional to $g^{1/4}$, too. That would be the case, e.g., if the emission line profiles were homologous. However, we want to revise this element of the comparison of theory with observation as well. Consequently, we compared the W_0 and W_1 widths to see, whether they are indeed analogous measurements of the chromospheric Ca II K line emission width, using our above described measurement method (see section 4.2)

Using the width measurements of the Ca II K emission line listed in Table 4, we compare and correlate W_1 with W_0 for our stellar sample. Fig. 6 shows this comparison, resulting in a linear least squares fit with a high Pearson's correlation coefficient of 0.934. The best relation for W_1 versus W_0 is

$$\log W_1 = (0.82 \pm 0.06) \log W_0 + (0.54 \pm 0.11). \quad (2)$$

This relation is not far from what one may expect of homologous emission line profiles (implying an exponent of 1.0), however it clearly proves that W_1 and W_0 scale differently over our sample. The effect is significant and must be taken into consideration by the comparison of theory with observation, see section below, in particular for the relation of line width with gravity.

5 GRAVITY AND TEMPERATURE DEPENDENCE: OBSERVATION VERSUS THEORY

The relation between the width of the Ca II K emission line and the stellar parameters, i.e. effective temperature and surface gravity, has been studied by a number of authors during the last decades (Reimers (1973), Neckel (1974), Ayres et al. (1975), Ayres (1979),

Table 4. Width measurements of the K emission line of Ca II.

Star	W_0^a [Å]	W_0^b [km/s]	$\log W_0^c$ [dex]	W_1^a [Å]	W_1^b [km/s]	$\log W_1^c$ [dex]
HD 8512	0.72	55	1.74 (0.07)	1.14	87.18	1.94 (0.04)
HD 10476	0.31	24	1.37 (0.16)	0.72	55.12	1.74 (0.07)
HD 18925	0.80	61	1.78 (0.06)	1.16	88.55	1.95 (0.04)
HD 20630	0.36	27	1.43 (0.14)	0.95	72.07	1.86 (0.05)
HD 23249	0.40	30	1.48 (0.12)	0.62	47.34	1.68 (0.08)
HD 26630	1.81	138	2.14 (0.03)	2.50	190.67	2.28 (0.02)
HD 27371	0.79	60	1.78 (0.06)	1.32	100.46	2.00 (0.04)
HD 27697	0.71	54	1.73 (0.07)	1.16	88.55	1.95 (0.04)
HD 28305	0.73	56	1.74 (0.07)	1.17	89.47	1.95 (0.04)
HD 28307	0.73	56	1.74 (0.07)	1.15	87.64	1.94 (0.04)
HD 29139	0.93	71	1.85 (0.05)	1.67	127.48	2.11 (0.03)
HD 31398	1.17	89	1.95 (0.04)	2.11	160.45	2.21 (0.02)
HD 31910	1.94	148	2.17 (0.03)	2.60	198.46	2.30 (0.02)
HD 32068	1.29	98	1.99 (0.04)	2.32	176.48	2.25 (0.02)
HD 48329	1.73	132	2.12 (0.03)	2.59	197.70	2.30 (0.02)
HD 71369	0.76	58	1.77 (0.06)	1.13	86.30	1.94 (0.04)
HD 81797	1.01	77	1.88 (0.05)	1.85	141.22	2.15 (0.03)
HD 82210	0.53	40	1.61 (0.09)	1.34	102.34	2.01 (0.04)
HD 96833	0.76	58	1.76 (0.07)	1.37	104.12	2.02 (0.04)
HD 104979	0.68	52	1.72 (0.07)	0.93	70.83	1.85 (0.05)
HD 109379	0.83	63	1.80 (0.06)	1.13	86.26	1.94 (0.04)
HD 114710	0.48	37	1.57 (0.10)	0.75	56.95	1.76 (0.07)
HD 115659	0.72	55	1.74 (0.07)	1.13	86.26	1.94 (0.04)
HD 124897	0.84	64	1.80 (0.06)	1.35	102.75	2.01 (0.04)
HD 148387	0.70	53	1.73 (0.07)	0.97	73.90	1.87 (0.05)
HD 159181	1.93	147	2.17 (0.03)	2.82	215.00	2.33 (0.02)
HD 164058	0.96	73	1.86 (0.05)	1.86	142.13	2.15 (0.03)
HD 186791	1.20	91	1.96 (0.04)	2.28	173.73	2.24 (0.02)
HD 198149	0.50	38	1.58 (0.10)	0.71	54.21	1.73 (0.07)
HD 204867	1.89	144	2.16 (0.03)	2.46	187.47	2.27 (0.02)
HD 205435	0.66	50	1.70 (0.08)	1.27	96.79	1.99 (0.04)
HD 209750	1.86	142	2.15 (0.03)	2.62	199.38	2.30 (0.02)

^a The error of the line width measurements is equivalent to the standard deviation of TIGRE-HEROS' instrumental line-profile close to K-line of Ca II ~ 0.11 Å.

^b The error in km/s is equivalent to 8 km/s.

^c Logarithmic values correspond to widths in km/s.

Lutz & Pagel (1982), Park et al. (2013)). The work of Ayres et al. (1975) demonstrated, how the Wilson-Bappu effect can be derived from of the relation of the chromospheric Ca II column density N with gravity g , assuming hydrostatic equilibrium at the bottom of the chromosphere. N in turn reflects on how the line width grows with lower gravity, by simple density-broadening – the migration of the photons into the line wings after multiple absorption and re-emission processes. Assuming also that the mean continuum optical depth in the stellar temperature minimum is relatively independent of surface gravity, Ayres et al. (1975) arrived at the simple relation $W_1 \propto A_{\text{met}}^{1/4} g^{-1/4}$, where A_{met} is the abundance of easily ionized metals relative to hydrogen. The simplification of the opacity problem, required to derive the above relation, was later supported by more detailed arguments, given in Ayres (1979) and Ayres (2019). A key point is, irrespective of, e.g., the relative proportions of H^- and line opacities in each chromosphere, that all relevant contributions to the opacity are controlled by the electron density in the same way.

We deliberately avoided studying the possible metallicity dependence, by the choice of a sample of mostly solar abundance, in order to have fewer ambiguity on the gravity dependence and to test the theoretical approach as such. A dependence of W_1 on T_{eff} was still

ignored by Ayres et al. (1975) because their initial stellar sample did not spread much over that parameter, only in gravity, but was then taken into consideration soon after by Ayres (1979). In consequence, the line broadening appears to depend on both, gravity and effective temperature. The latter effect is based on the ionization ratio of Ca I:Ca II, consequently reducing the Ca II column density in the coolest chromospheres (comparing stars of same surface gravity). Still this is of secondary nature because the range of effective temperatures of cool stars with chromospheres is quite limited, while gravity covers more than four orders of magnitude.

There is now a problem with any empirical assessment of the line width relation, simultaneously with both these parameters: cross-talk from a mismatch of the effective temperature affecting the gravity term. That interrelation is caused by the orientation of the giant branches in the HR diagram: the coolest giants are also mostly those with the highest luminosity and, consequently, lowest gravity. Hence, to empirically evaluate the theoretical reasoning of Ayres et al. (1975) by means of the gravity term of the emission line width, one must get the temperature term right as well.

To test the interpretation of the Wilson-Bappu effect by Ayres et al. (1975) and Ayres (1979), we derived the width correlation of the Ca II K emission line with surface gravity and effective tempera-

Table 5. Results for the gravity and temperature dependence of the WBE considering different measurements of the K emission line of Ca II.

Width	α	β	C	χ^2
W_0	-0.279 (0.011)	2.93 (0.22)	-8.3 (0.8)	0.0360
W_1	-0.220 (0.020)	1.8 (0.4)	-4.1 (1.4)	0.1040
W'_1	-0.229 (0.009)	2.41 (0.18)	-6.3 (0.7)	0.0216

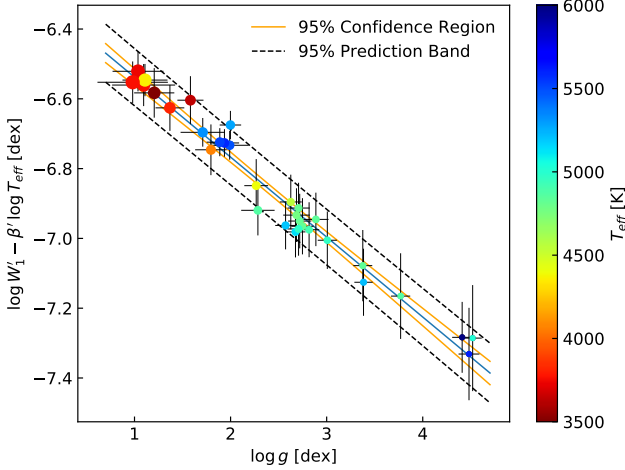


Figure 7. Dependence of W'_1 on $\log g$ by subtracting the temperature contribution. The blue line corresponds to a linear fit. The color code represents the effective temperature, and the point-size represents the surface gravity, using larger points for lower gravities.

ture in our sample, for both measurements, W_0 and W_1 , using simple power-law relations in their logarithmic form:

$$\log W = \alpha \log g + \beta \log T_{\text{eff}} + C. \quad (3)$$

where α , β and C are fitting constants. Table 5 shows the results for these values when we apply equation 3 to W_0 and W_1 .

Based on the best χ^2 , we observe that W_0 has a better correlation with gravity and temperature than W_1 for our stellar sample. However, this can be explained by the better definition of the former on the flanks of line profile. And as we showed in subsection 4.3, there is a clear relation between both widths, where W_0 rises a bit faster than W_1 (see equation 2). Therefore, the relation of $\log W_1$ has a smaller power with $\log g$ than $\log W_0$.

We may also convert W_0 into W_1 values, using equation 2, in order to circumnavigate the larger uncertainties of individual W_1 values. We tested the dependence of these converted values W'_1 with gravity and temperature in the same way as before and found that their correlation got two times better than W_0 , based on the respective minimal χ^2 sums. In addition, the gravity exponent calculated with W'_1 is the closest to the theoretical prediction of Ayres et al. (1975). This is pictured in Fig. 7 and Fig. 8, showing the direct dependence of $\log W'_1$ with $\log g$, as well as $\log T_{\text{eff}}$, subtracting the respective other contribution.

6 CONCLUSIONS

We developed and demonstrated a consistent analysis, applied uniformly on a representative stellar sample, for which we obtained

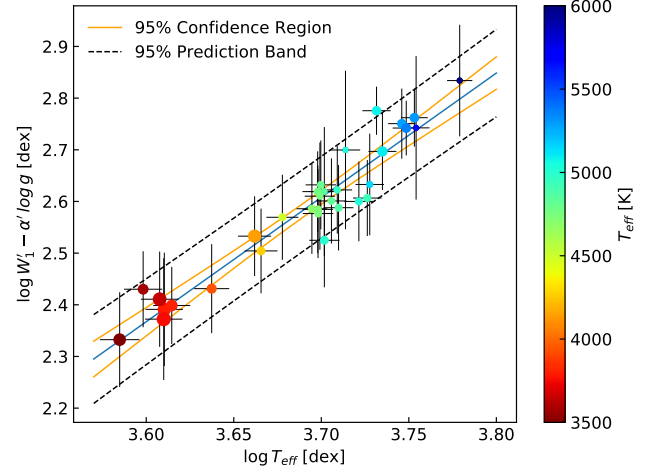


Figure 8. Dependence of W'_1 on $\log T_{\text{eff}}$ by subtracting the gravity contribution. The blue line corresponds to a linear fit. The color code represents the effective temperature, and the point-size represents the surface gravity with larger points for lower gravities.

good S/N TIGRE spectra of the moderately high spectral resolving power of $R \sim 20,000$. The new Gaia EDR3 parallaxes allowed us to calculate precise, parallax-based gravities, in combination with stellar mass estimates based on HRD-position matching evolution tracks. That approach facilitated the assessment of effective temperatures by means of spectral synthesizing, as we were able to exclude false solutions with erroneous gravities.

Furthermore, with the help of our here presented measurement technique for the chromospheric Ca II K emission line width, we found that the width used by O.C. Wilson, W_0 (the width at half-peak intensity), and the width of theoretical significance, W_1 (the K_1 minima separation, originating in the temperature minimum at the very bottom of the chromosphere), do not scale 1:1 across the HRD, but are related to each other by $\log W_1 = 0.82 \log W_0 + 0.53$. Hence, chromospheric emission lines are not exactly homologous over a wider range of gravity. Therefore, the relation between W_0 and W_1 is required to extend the empirical Wilson-Bappu effect, based on W_0 , to a relation of the line width with physical parameters such as gravity and effective temperature, as predicted by theory for W_1 .

This distinction and the above described consistent approach to the physical parameter assessment for our sample stars, enables us to test the theoretical explanation of Ayres et al. (1975) and Ayres (1979), in particular by comparing the empirical findings to their predicted gravity dependence. In fact, ignoring the difference between the two emission line widths leads to a much worse agreement of theory with observation.

In conclusion, we confirm the dependence on gravity proposed by Ayres et al. (1975) and Ayres (1979), suggesting that the Wilson-Bappu effect is indeed a line saturation and photon redistribution effect, driven by the growing column densities in giants with lower gravities. That same interpretation provides a straight-forward explanation for the temperature term as well, namely the effect of the Ca II:Ca I ionization balance. Even though it is difficult to quantify, because (i) the relevant temperature of the line-forming layers of each chromosphere cannot so easily be related to the effective temperature of the respective stellar photosphere underneath, and (ii) because of NLTE effects in any chromospheric ionization balance, the intuitive understanding is that cooler stars have a larger fraction

of neutral Ca in their chromospheres, resulting in a reduced Ca II column density. This explains the positive sign of the temperature exponent, while the substantial effect over a relatively small temperature range calls for a large value – as observed.

This nice agreement of our empirical study with the theoretical predictions of Ayres et al. (1975) also suggests the validity, at least to a good degree, of their assumption of hydrostatic equilibrium at the base of the chromosphere – at least for stars, that are not overly active. In those cases, the chromospheric structure is not dominated by magnetic energy density and its dynamic fine structure. This is good news: chromospheric physics may not be entirely hopeless – after all, some approximations do appear to be reasonable. At least, this is our interpretation of the meaning of the Wilson-Bappu effect and the agreement obtained with simple chromospheric physics.

ACKNOWLEDGEMENTS

This study used the services of the Strasbourg astronomical data centre, and data from the European Space Agency (ESA) mission *Gaia* (<https://www.cosmos.esa.int/gaia>), processed by the *Gaia* Data Processing and Analysis Consortium (DPAC, <https://www.cosmos.esa.int/web/gaia/dpac/consortium>). Furthermore, this study made use of the *Gaia* FGK Benchmark Stars Library <https://www.blancocuaresma.com/s/benchmarkstars>.

We wish to thank Thomas Ayres for his very helpful comments on the subject of this publication, prior to submission. Furthermore, we are grateful to Marco Mittag from the University of Hamburg for his permission to use the TIGRE spectra of HD 198149 and HD 20630 of his observing program. The authors also wish to acknowledge the valuable work of Sergi Blanco-Cuaresma, CfA, Harvard-Smithsonian, on ISPEC, a very useful tool for spectral analysis and parameter synthesis. We are grateful to the referee, Jeffrey L. Linsky, for his valuable recommendations of additional literature and more. We also appreciate the suggestions of the editor Dr. Helen Klus that improved the quality of our work.

This work benefited from financial support of the bilateral project CONACyT-DFG No. 278156 for the TIGRE collaboration with the University of Hamburg, and from general support of our home institutions. In particular, we thank the University of Guanajuato for the grants for the projects 036/2021 and 105/2021 of the *Convocatoria Institucional de Investigación Científica 2021 and 2022*.

DATA AVAILABILITY

The data underlying this article are available in the article.

REFERENCES

- Alvarez R., Plez B., 1997, *A&A*, 330, 1109
 Aurière M., et al., 2015, *A&A*, 574, A90
 Ayres T. R., 1979, *ApJ*, 228, 509
 Ayres T. R., 2019, in , *The Sun as a Guide to Stellar Physics*. Elsevier, pp 27–57, doi:10.1016/B978-0-12-814334-6.00002-9
 Ayres T. R., Shine R. A., Linsky J. L., 1975, *ApJ*, 195, L121
 Blanco-Cuaresma S., 2019, *MNRAS*, 486, 2075
 Blanco-Cuaresma S., Soubiran C., Jofré P., Heiter U., 2014a, *A&A*, 566, 1
 Blanco-Cuaresma S., Soubiran C., Heiter U., Jofré P., 2014b, *A&A*, 569, A111
 Catanzaro G., 1997, *Ap&SS*, 257, 161
 Cram L. E., Ulmschneider P., 1978, *A&A*, 62, 239

- Czesla S., 2014, Technical Report 1, The instrumental line-profile of TIGRE/HEROS. Hamburger Sternwarte, Hamburg, Germany
 ESA 1997, The Hipparcos and Tycho Catalogues. ESA SP-1200
 Eberhard G., Schwarzschild K., 1913, *ApJ*, 38, 292
 Flower P. J., 1996, *ApJ*, 469, 355
 Gaia Collaboration et al., 2016, *A&A*, 595, 1
 Gaia Collaboration et al., 2021, *A&A*, 649, A1
 Grevesse N., Asplund M., Sauval A. J., 2007, *Space Sci. Rev.*, 130, 105
 Gustafsson B., Edvardsson B., Eriksson K., Jørgensen U. G., Nordlund Å., Plez B., 2008, *A&A*, 486, 951
 Hawkins K., et al., 2016, *A&A*, 592, 1
 Heiter U., Jofré P., Gustafsson B., Korn A. J., Soubiran C., Thévenin F., 2015, *A&A*, 582, 1
 Husser T. O., Wende-von Berg S., Dreizler S., Homeier D., Reiners A., Barman T., Hauschildt P., 2013, *A&A*, 553, 1
 Jofré P., et al., 2014, *A&A*, 564, 1
 Jofré P., et al., 2015, *A&A*, 582, 1
 Jofré P., et al., 2017, *A&A*, 601, 1
 Lindegren L., et al., 2021, *A&A*, 649, A2
 Linsky J. L., 2017, *ARA&A*, 55, 159
 Linsky J. L., Avrett E. H., 1970, *PASP*, 82, 169
 Lutz T. E., 1970, *AJ*, 75, 1007
 Lutz T. E., Pagel B. E. J., 1982, *MNRAS*, 199, 1101
 Montes D., Fernandez-Figueroa M. J., de Castro E., Cornide M., 1994, *A&A*, 285, 609
 Neckel H., 1974, *A&A*, 35, 99
 Park S., Kang W., Lee J. E., Lee S. G., 2013, *ApJ*, 146, 73
 Piskunov N. E., Kupka F., Ryabchikova T., Weiss W. W., Jeffery C. S., 1995, *A&AS*, 112, 525
 Plez B., 2012, Turbospectrum: Code for spectral synthesis
 Pols O. R., Tout C. A., Schröder K. P., Eggleton P. P., Manners J., 1997, *MNRAS*, 289, 869
 Pols O. R., Schröder K. P., Hurley J. R., Tout C. A., Eggleton P. P., 1998, *MNRAS*, 298, 525
 Reimers D., 1973, *A&A*, 24, 79
 Ryabchikova T., et al., 2016, *MNRAS*, 456, 1221
 Schmitt J. H. M. M., et al., 2014, *Astron. Nachr.*, 335, 787
 Schröder K. P., Pols O. R., Eggleton P. P., 1997, *MNRAS*, 285, 696
 Schröder K. P., Mittag M., Hempelmann A., Schmitt J. H. M. M., 2013, *A&A*, 554, A50
 Schröder K. P., Schmitt J. H. M. M., Mittag M., Gómez-Trejo V., Jack D., 2018, *MNRAS*, 480, 2137
 Schröder K. P., Mittag M., Jack D., Jiménez A. R., Schmitt J. H. M. M., 2020, *MNRAS*, 492, 1110
 Schröder K. P., Mittag M., Flor Torres L. M., Jack D., Snellen I., 2021, *MNRAS*, 501, 5042
 Shine R. A., Milkey R. W., Mihalas D., 1975, *ApJ*, 201, 222
 Soubiran C., Le Campion J. F., Brouillet N., Chemin L., 2016, *A&A*, 591, 1
 Torres G., 2010, *AJ*, 140, 1158
 Wilson O. C., 1967, *PASP*, 79, 46
 Wilson O. C., Bappu M. K. V., 1957, *ApJ*, 125, 661

APPENDIX A: PSEUDO-CONTINUUM READJUSTMENT AND LINE SELECTION FOR SYNTHESIZING PROCEDURE WITH ISPEC

A1 Guided readjustment of the pseudo-continuum

To find suitable continuum sections, which are needed to guide the readjustment of the pseudo-continuum of the observed spectrum, ideally at the value of 1.0, we used a synthetic spectrum that matches the observed spectrum reasonably well. To produce it, the initial values of T_{eff} , $\log g$ and $[\text{Fe}/\text{H}]$ were set to the averages of the respective entries in the PASTEL catalogue. Furthermore, the resolution of the synthetic spectrum was set to the one of the TIGRE-HEROS target spectrum ($R \sim 20,000$), and the projected rotation velocity $v \sin i$

was fixed at the small value of 1.6 km/s. This is a reasonable choice for giants, as well as for aged and relatively inactive main sequence stars, which form our sample. Individual differences of a few km/s in this rotation rate cannot be resolved by TIGRE-HEROS spectra, anyway.

At this point, another choice was required, namely for the initial values of micro and macro turbulent velocities. Despite these being below the resolution limit of TIGRE-HEROS spectra, their choices make subtle but systematic differences in the χ^2 sums of later best-fit solutions. Therefore, in the final synthesizing of the physical parameters (see below), the turbulence values are allowed to be refined, see Table 1. But for the initial model spectrum required here only to define suitable continuum sections, we needed reasonable fixed values.

Initially, we tested the macro and micro-turbulence velocities, v_{mac} and v_{mic} , used for the models of the PHOENIX library (Husser et al. 2013), which give reasonably realistic spectra for stars with solar abundances, over a range of effective temperatures and surface gravities. Therefore, like (Husser et al. 2013), we first fixed the macro-turbulence parameters at twice the micro-turbulence values. However, after several tests with well-studied stars (see subsection 3.4), we refined the initial choices of macro-turbulence velocity v_{mac} by the following empirical representation, according to the findings in main sequence stars by Ryabchikova et al. (2016), while still using the micro-turbulence values of Husser et al. (2013) in this step:

$$v_{\text{mac}} = \begin{cases} 2.00v_{\text{mic}} & \text{if } \log g \leq 2.0 \\ 3.00v_{\text{mic}} & \text{if } 2.0 < \log g < 3.75 \\ 3.75v_{\text{mic}} & \text{if } \log g \geq 3.75. \end{cases} \quad (\text{A1})$$

In this so-defined, representative synthetic spectrum, we then selected continuum sections according to the following criteria: (1) Maximum standard deviation from 1.0 of 0.1 per cent, and (2) minimum size of the region equivalent to FWHM of the instrumental profile of TIGRE-HEROS ($\sim 0.35 \text{ \AA}$ in the center of R-channel, $\sim 0.23 \text{ \AA}$ in the centre of B-channel). (3) To avoid confusion, spectral regions with abundant telluric lines were also discarded (Catanzaro 1997).

These continuum sections were finally used to readjust the observed stellar pseudo-continuum, employing the ISPEC algorithm designed for this. According to Blanco-Cuaresma et al. (2014b), this subroutine applies a median and maximum filter with different window sizes. The former smooths out the noise in the continuum, while the latter ignores slightly smaller fluxes, which rather belong to shallow absorption lines – i.e., the continuum may effectively be placed slightly above or below the simple flux average in the respective continuum section, depending on the values of those parameters. Then, this algorithm applies a third-degree spline, assigning one node every 20 \AA only within these selected continuum regions. This procedure is repeated recursively to different median and maximum filters, ten steps for each one from 0.1 \AA to 1.0 \AA for the first, and 1.5 \AA to 15 \AA for the last one. A total of up to 100 possible normalizations are calculated.

The script finds the residuals between the synthetic and observed spectrum, and calculates the RMS only in the continuum regions. The readjusted spectrum with the best RMS is finally chosen. Finally, a second fine-tuning normalization is applied to the observed spectrum. Using again the continuum sections, this time as a template in the observed spectrum, the ISPEC script further improves the normalization by the use of a median filter equal to the instrumental profile width of TIGRE-HEROS. As a whole, this guided continuum readjustment procedure improves the original normalization of the

observed spectrum significantly, because the former can be misled by agglomerations of absorption lines.

A2 Selection of representative lines for synthesizing procedure

We selected a representative, reliable subset of lines for the synthesizing procedure, aiming on small χ^2 minima, less impacted by line blends or mismatching atomic line strengths (f -values). For our sample stars, we based that selection on the following criteria: (1) the S/N in each line must be greater than 5 times; (2) a cross correlation is undertaken between the information of the Vienna Atomic Line Data Base (VALD) (Piskunov et al. 1995) and the observed lines, avoiding differences in wavelength larger than the width of the instrumental profile of TIGRE-HEROS ($\sim 0.35 \text{ \AA}$); (3) lines within spectral regions known to host many telluric lines are discarded; (4) were the observed line strength disagrees with the atomic data of the VALD list, or would even be zero according to the synthetic spectrum, such lines are discarded (see below).

We applied these criteria to a good solar spectrum, taken by TIGRE-HEROS, using a strategy similar to the line-by-line differential approach of Blanco-Cuaresma (2019), that is: a line can be considered good, when synthesizing arrives at a close-to-solar abundance (i.e. reasonably close to zero). After several tests, if a spectral element has more than 20 lines, we considered an abundance mismatch-margin of ± 0.15 dex, otherwise accepted a margin of ± 0.50 dex. Hence, lines producing an error larger than 0.50 dex are discarded. This tolerated metallicity mismatch, reflecting atomic data mismatches of the line list, is a compromise between quantity and quality of the selection. By this approach, only lines from iron peak elements (iron, chromium, nickel) and alpha elements (silicon, calcium, titanium) would qualify. For the here required solar reference model, we used the solar parameters¹ to $T_{\text{eff}} = 5772 \text{ K}$, $\log g = 4.44$ dex and $[\text{M}/\text{H}] = 0.00$ dex. Again the initial v_{mic} was determined using the PHOENIX library, v_{mac} with equation A1, and $v \sin i$ was fixed to 1.6 km/s.

From this process, a total of 202 lines were selected for the R-channel spectra of HEROS (covering 5800 to 8700 \AA). The final line list is shown in Table A1. In the same way of Blanco-Cuaresma (2019), these lines are not blindly used on the observed spectra. Before starting the parameter synthesizing process, the script checks if each of these lines exists in the target spectrum, and using a gaussian fit, then applies the equivalent width criterion as stated above, before including the line in the process. According to our tests, these lines worked well enough for our sample from main sequence stars to supergiants (see subsection 3.4).

APPENDIX B: CA II EMISSION LINE WIDTH MEASUREMENTS OF THE STELLAR SAMPLE

We present the Ca II emission line width measurements of the stellar sample with a fixed wavelength scale to comparison purposes. Fig. B1 shows the measurements for HD 8512, HD 10476, HD 18925, HD 20630, HD 23249, HD 26630, HD 27371 and HD 27697. Fig. B2 for HD 28305, HD 28307, HD 29139, HD 31398, HD 31910, HD 32068, HD 48329 and HD 71369. Fig. B3 for HD 81797, HD 82210, HD 96833, HD 104979, HD 109379, HD 114710, HD 115659 and HD 124897. Fig. B4 for HD 148387, HD 159181, HD 164058, HD

¹ Values from NASA Sun Fact Sheet <https://nssdc.gsfc.nasa.gov/planetary/factsheet/sunfact.html>

Table A1. List of lines selected for use with the iSPEC script.

λ_0 [nm]	λ_{blue} [nm]	λ_{red} [nm]	Note
580.52548	580.48018	580.55266	Ni 1
580.57078	580.55266	580.61608	Fe 1
580.67044	580.61608	580.73386	Fe 1
580.92412	580.84258	581.01472	Fe 1
581.47677	581.43147	581.55831	Fe 1
581.63079	581.57643	581.67609	Fe 1
583.16193	583.10757	583.21629	Ni 1
583.83236	583.78706	583.89578	Fe 1
584.70212	584.64776	584.75648	Ni 1
584.81084	584.75648	584.85614	Fe 1
585.74402	585.64436	585.81650	Ca 1
585.96145	585.90709	586.04299	Fe 1
586.64095	586.58659	586.68625	Ti 1
586.75873	586.68625	586.79497	Ca 1
587.32045	587.26609	587.35669	Fe 1
592.77455	592.72925	592.81079	Fe 1
593.01916	592.98292	593.07352	Fe 1
593.46310	593.41780	593.51746	Fe 1
595.27510	595.21168	595.37475	Fe 1
596.58879	596.51631	596.63409	Ti 1
597.85718	597.82094	597.92966	Ti 1
598.48232	598.43702	598.58198	Fe 1
599.13464	599.09840	599.16182	Fe 2
599.67824	599.62388	599.70542	Ni 1
600.72919	600.68389	600.75637	Ni 1
600.79261	600.75637	600.81979	Fe 1
604.20822	604.11762	604.28070	Fe 1
605.36789	605.31353	605.47661	Ni 1
605.60345	605.55815	605.67593	Fe 1
606.54569	606.50039	606.62723	Fe 1
608.41204	608.33956	608.45734	Fe 2
608.52076	608.45734	608.57512	Fe 1
608.62948	608.57512	608.72008	Ni 1
609.11872	609.07342	609.14590	Ti 1
609.36334	609.32710	609.39958	Fe 1
609.82539	609.78915	609.94317	Fe 1
610.26933	610.24215	610.30557	Ca 1
610.32369	610.30557	610.41429	Fe 1
612.21722	612.12662	612.30782	Ca 1
612.49808	612.42560	612.56150	Si 1
612.62492	612.56150	612.67928	Ti 1
612.78800	612.71552	612.85142	Fe 1
612.89672	612.85142	612.94202	Ni 1
613.17758	613.08698	613.26818	Si 1
613.66682	613.61246	613.73024	Fe 1
614.24665	614.21947	614.29195	Si 1
614.50033	614.44597	614.58187	Si 1
614.78119	614.69965	614.82649	Fe 1
614.92615	614.88085	614.97145	Fe 2
615.16171	615.10735	615.20701	Fe 1
615.76873	615.70531	615.85933	Fe 1
616.13113	616.10395	616.16737	Ca 1
616.22173	616.16737	616.29421	Ca 1
616.35763	616.29421	616.42105	Ca 1
616.53882	616.49352	616.59318	Fe 1
616.64754	616.59318	616.73814	Ca 1
616.90122	616.81968	616.92840	Ca 1
616.95558	616.92840	617.00994	Ca 1
617.05524	617.00994	617.16396	Fe 1
617.33610	617.27268	617.38140	Fe 1

Table A1 – continued List of lines selected for use with the iSPEC script.

λ_0 [nm]	λ_{blue} [nm]	λ_{red} [nm]	Note
617.53542	617.45388	617.58978	Ni 1
617.68038	617.61696	617.78004	Ni 1
618.02466	617.97030	618.07902	Fe 1
618.35988	618.30552	618.42330	Fe 1
619.15715	619.04843	619.27493	Fe 1
619.54673	619.50143	619.60109	Si 1
620.03597	619.98161	620.08127	Fe 1
621.34060	621.28624	621.42214	Fe 1
622.02916	621.97480	622.04728	Ti 1
622.40062	622.33720	622.43686	Ni 1
622.67242	622.59088	622.71772	Fe 1
622.92610	622.85362	622.97140	Fe 1
623.00764	622.97140	623.02576	Ni 1
623.07106	623.02576	623.16166	Fe 1
623.73243	623.57841	623.78679	Si 1
623.84115	623.78679	623.89551	Fe 2
624.06765	623.95893	624.11295	Fe 1
624.38475	624.33945	624.41193	Si 1
624.62937	624.58407	624.69279	Fe 1
624.75621	624.69279	624.81057	Fe 2
625.25451	625.20921	625.31793	Fe 1
625.80717	625.77093	625.83435	Ti 1
625.87059	625.83435	625.91588	Ti 1
625.96118	625.91588	626.01554	Ni 1
626.10614	626.05178	626.16956	Ti 1
627.02120	626.95778	627.07556	Fe 1
627.12992	627.07556	627.16616	Fe 1
630.14689	630.09253	630.21031	Fe 1
631.14348	631.08912	631.18878	Fe 1
631.57836	631.56024	631.62366	Fe 1
632.21256	632.16726	632.23068	Ni 1
632.26692	632.23068	632.32128	Fe 1
633.00983	632.93736	633.04607	Cr 1
633.68027	633.62591	633.77087	Fe 1
633.89771	633.81617	633.97019	Ni 1
635.86372	635.81842	635.93620	Fe 1
636.28954	636.26236	636.38920	Fe 1
636.44356	636.38920	636.52510	Fe 1
636.64288	636.58852	636.69724	Ni 1
636.95092	636.86032	636.98716	Fe 2
637.13212	637.07776	637.20460	Si 2
637.82973	637.77537	637.92033	Ni 1
638.07435	638.01999	638.14683	Fe 1
638.46393	638.41863	638.50923	Ni 1
638.56359	638.50923	638.61795	Fe 1
639.26121	639.17061	639.28839	Fe 1
639.36087	639.28839	639.47865	Fe 1
640.00412	639.90447	640.08566	Fe 1
640.72892	640.63832	640.75610	Si 1
641.16380	641.04602	641.23628	Fe 1
641.49902	641.40842	641.59868	Si 1
641.68928	641.62586	641.73458	Fe 2
641.99732	641.90672	642.05168	Fe 1
642.13322	642.07886	642.20570	Fe 1
642.48655	642.42313	642.53185	Ni 1
643.08451	643.00297	643.13887	Fe 1
643.90897	643.83649	644.02675	Ca 1
644.97804	644.94180	645.09582	Ca 1
645.55788	645.52164	645.59412	Ca 1
645.63942	645.59412	645.67566	Fe 2

Table A1 – *continued* List of lines selected for use with the iSPEC script.

λ_0 [nm]	λ_{blue} [nm]	λ_{red} [nm]	Note
646.26456	646.20114	646.31892	Ca 1
649.15469	649.11845	649.21811	Ti 2
649.38119	649.33589	649.41742	Ca 1
649.49896	649.41742	649.54426	Fe 1
649.65298	649.61674	649.66204	Fe 1
649.89760	649.84324	649.92478	Fe 1
649.96102	649.92478	650.05162	Ca 1
659.75484	659.69142	659.80920	Fe 1
660.91452	660.85110	661.01418	Fe 1
662.50001	662.44565	662.54531	Fe 1
662.75369	662.68121	662.79899	Fe 1
663.51473	663.46037	663.55096	Ni 1
663.97678	663.92242	664.04020	Fe 1
664.69252	664.65628	664.74688	Fe 1
666.11493	666.06057	666.16929	Cr 1
666.76725	666.70383	666.81255	Fe 1
667.80009	667.69137	667.85445	Fe 1
671.03449	670.98919	671.09791	Fe 1
671.62339	671.57809	671.66869	Fe 1
672.53845	672.49315	672.59281	Fe 1
672.66529	672.59281	672.75589	Fe 1
674.31420	674.23266	674.42292	Ti 1
675.01182	674.95746	675.07524	Fe 1
675.27456	675.20208	675.31985	Fe 1
677.23151	677.16809	677.30399	Ni 1
679.35154	679.27000	679.40590	Fe 1
680.68335	680.61993	680.74677	Fe 1
681.02763	680.97327	681.08199	Fe 1
682.85774	682.73996	682.93928	Fe 1
683.70032	683.61878	683.79998	Fe 1
683.98118	683.93588	684.02648	Fe 1
684.13520	684.02648	684.17144	Fe 1
684.20768	684.17144	684.23486	Ni 1
684.36170	684.31640	684.43418	Fe 1
685.51231	685.39453	685.64821	Fe 1
685.81129	685.76599	685.89283	Fe 1
686.24617	686.21899	686.32771	Fe 1
743.07931	743.01589	743.12461	Fe 1
744.30240	744.24804	744.38394	Fe 1
744.93660	744.85506	744.98190	Fe 2
745.39866	745.33524	745.46208	Fe 1
746.15063	746.09627	746.18687	Fe 1
746.23217	746.18687	746.29559	Cr 1
747.35561	747.31031	747.40997	Fe 1
748.19819	748.09853	748.27066	Fe 1
749.16760	749.10418	749.26726	Fe 1
750.60813	750.55378	750.66249	Fe 1
751.10643	750.92523	751.20609	Fe 1
752.27517	752.20269	752.36577	Ni 1
752.51073	752.44731	752.58321	Ni 1
754.18682	754.09622	754.24118	Fe 1
757.40311	757.35781	757.48465	Ni 1
758.38158	758.27286	758.46312	Fe 1
772.75974	772.68726	772.83222	Ni 1
774.55361	774.47207	774.61703	Fe 1
774.65327	774.61703	774.71669	Fe 1
774.82541	774.71669	774.86165	Fe 1
774.88883	774.86165	774.95225	Ni 1
775.11533	775.03379	775.20593	Fe 1
776.05757	775.99415	776.19347	Si 1

Table A1 – *continued* List of lines selected for use with the iSPEC script.

λ_0 [nm]	λ_{blue} [nm]	λ_{red} [nm]	Note
780.78687	780.70533	780.85935	Fe 1
784.99975	784.90915	785.06317	Si 1
785.53429	785.47993	785.62489	Fe 1
846.84305	846.77057	846.96989	Fe 1
847.16920	847.07860	847.29604	Fe 1
848.19298	848.12050	848.26546	Fe 1
849.80565	849.46137	850.09557	Ca 2
851.40927	851.34585	851.46363	Fe 1
851.50893	851.46363	851.57235	Fe 1
851.83508	851.77167	851.89850	Ti 1
855.67651	855.59497	855.82147	Si 1
858.23142	858.13176	858.28578	Fe 1
859.59041	859.52699	859.65383	Si 1
859.70819	859.65383	859.78067	Si 1
859.88033	859.78067	859.97093	Fe 1
861.17591	861.11249	861.23932	Fe 1
862.16344	862.10002	862.22686	Fe 1
863.69457	863.65833	863.75799	Ni 1
867.47258	867.40916	867.65378	Fe 1
868.64131	868.54165	868.72285	Si 1
868.85875	868.72285	868.94935	Fe 1
869.94595	869.90065	869.98219	Fe 1

186791, HD 198149, HD 204867, HD 205435 and HD 209750. The blue line represents the fit using cubic splines, the dashed line is the half intensity of the peak and gray zone is the measurement uncertainty.

This paper has been typeset from a \LaTeX file prepared by the author.

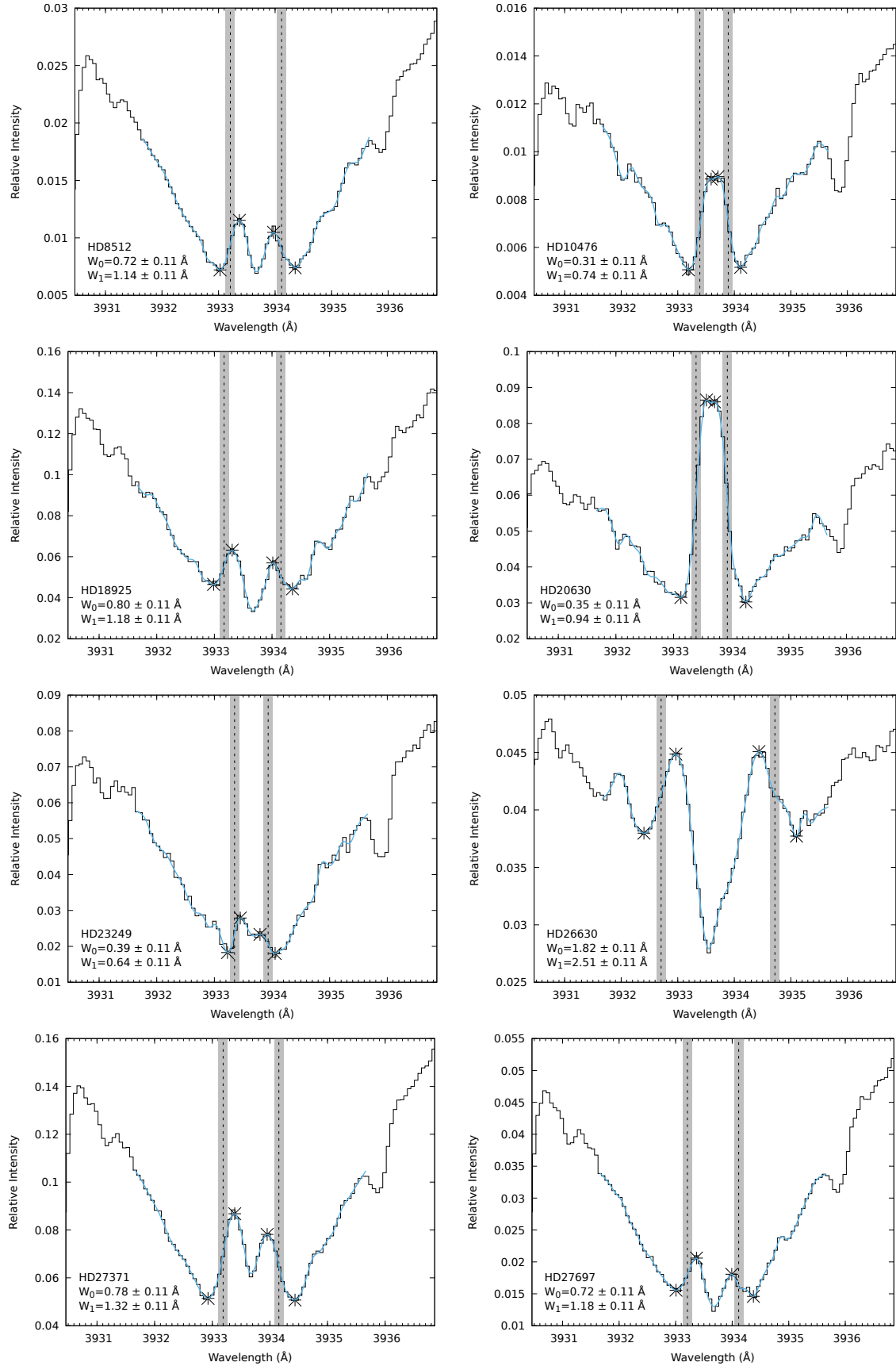


Figure B1. Ca II emission line width measurements of HD 8512, HD 10476, HD 18925, HD 20630, HD 23249, HD 26630, HD 27371 and HD 27697.

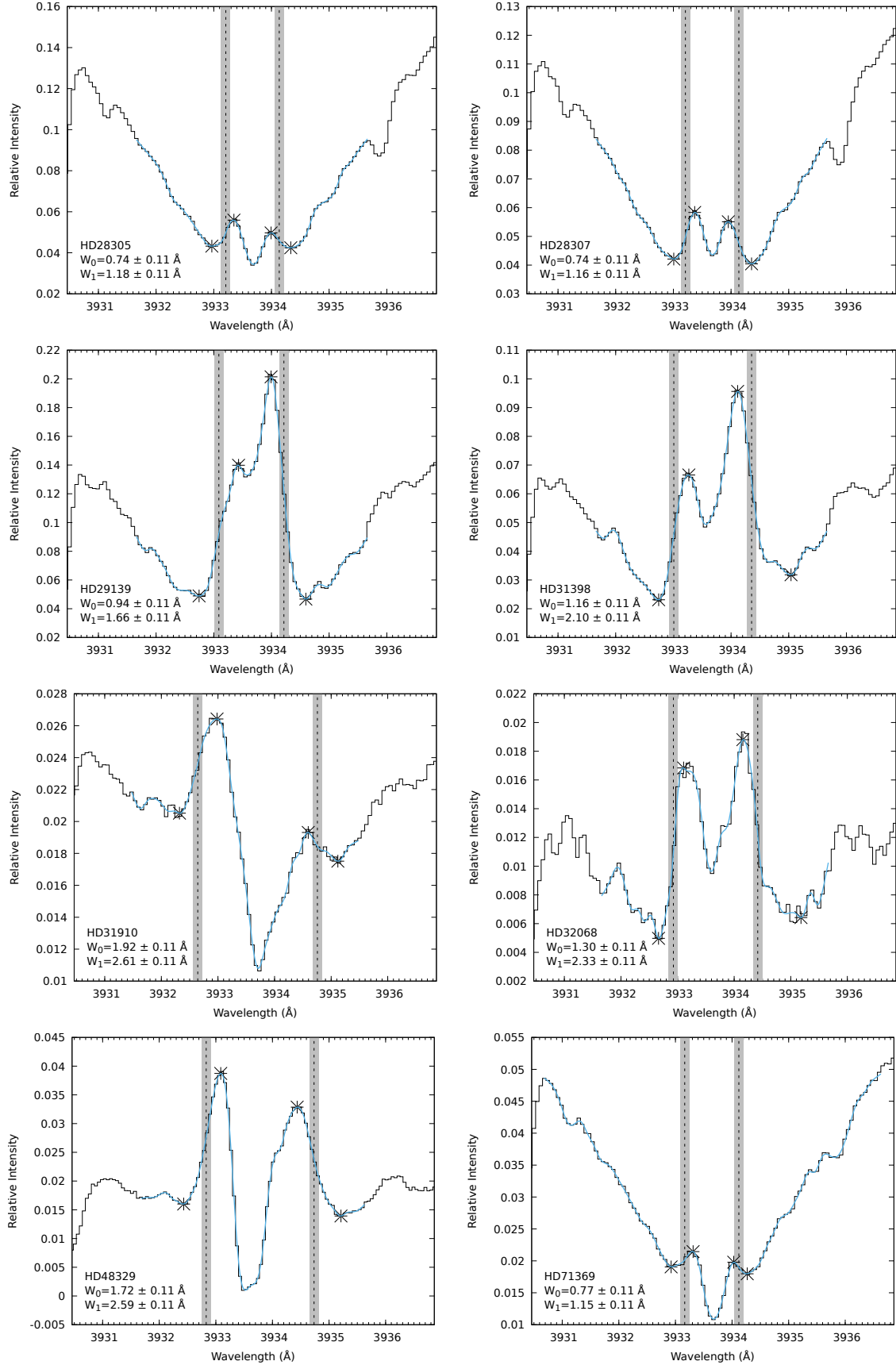


Figure B2. Ca II emission line width measurements of HD 28305, HD 28307, HD 29139, HD 31398, HD 31910, HD 32068, HD 48329 and HD 71369.

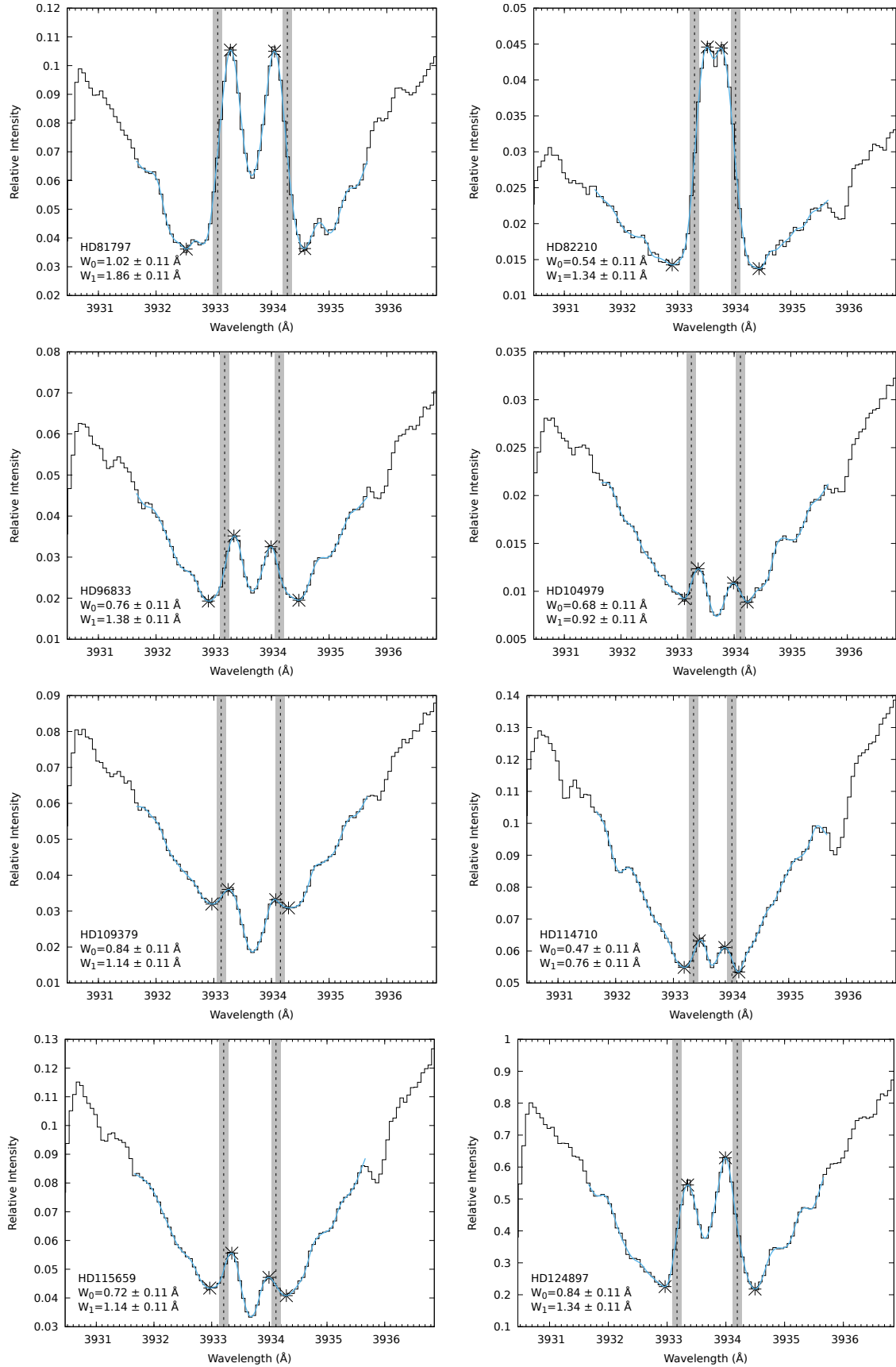


Figure B3. Ca II emission line width measurements of HD 81797, HD 82210, HD 96833, HD 104979, HD 109379, HD 114710, HD 115659 and HD 124897.

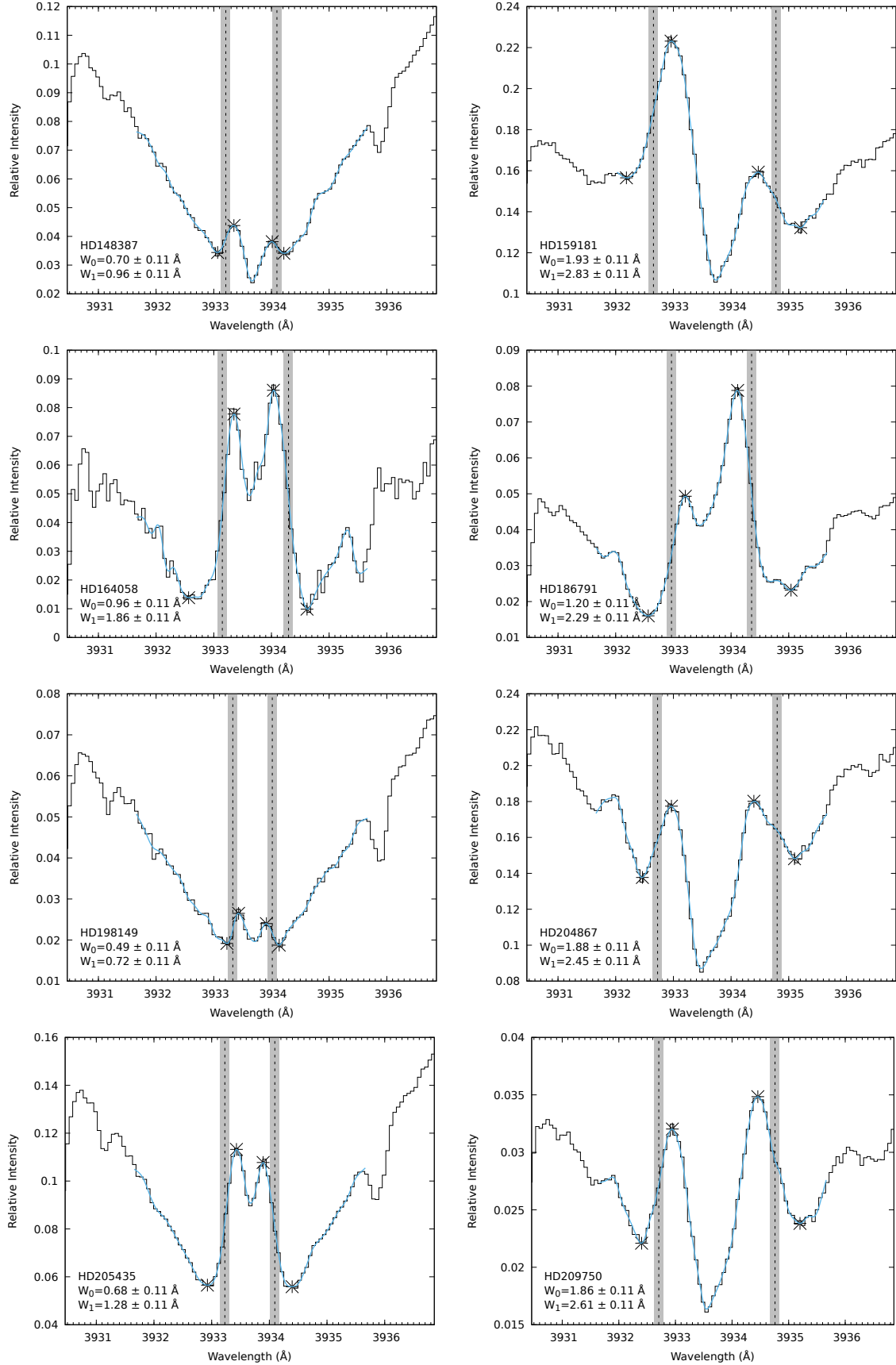


Figure B4. Ca II emission line width measurements of HD 148387, HD 159181, HD 164058, HD 186791, HD 198149, HD 204867, HD 205435 and HD 209750.